# Evaluation of SiC cladded annular fuel as accident tolerant fuel for PWRs


## NA Mashilangako

orcid.org/0000-0002-0771-612X


Dissertation accepted in fulfilment of the requirements for the degree *Master of Sciences in Engineering Sciences with Nuclear Engineering* at the North-West University

Supervisor: Dr MH du Toit

Co-supervisor: Prof F van Niekerk

Graduation: JUNE 2023

Student number: 28566319

# DECLARATION

I, Ngoatladi A Mashilangako, hereby declare that I have formed, completed, and written the dissertation Evaluation of SiC cladded annular fuel as accident tolerant fuel for PWRs. It was not previously submitted for any degree to any tertiary institution.

Name: Ngoatladi A Mashilangako

Signature:

Date:

# ABSTRACT

Nuclear energy produced by Light Water Reactors (LWRs) was in the spotlight in the aftermath of the Fukushima disaster, which led to the development of Accident Tolerant Fuels (ATF). ATF desires to improve fuel safety and performance under normal and accident operating conditions. This dissertation focuses on contributing research towards ATFs and nuclear reactor safety.

The study aimed to develop the North Anna (reference) 3D fuel pin and assembly models. The reference reactor uses a solid fuel pin ($UO_2$ pellets) and Zircaloy cladding, and the study seeks to replace the solid fuel pin with annular fuel pins and the cladding with Silicon Carbide (SiC). Two types of annular fuel pins were developed, the water annulus fuel pin and the helium annulus fuel pin. This study is unique because most studies modelled the water annulus fuel pin, whereas the helium annulus fuel pin was developed for this study.

Serpent 2.1.0, a continuous-energy, burnup and neutronics code and the Computational Fluid Dynamics (CFD) simulation code Flownex 8.12.8 were coupled externally. An iterative process was used between the two codes to achieve power distribution, fuel temperature, coolant temperature and density convergence. The adaptive relaxation method is applied to prevent divergence between iterations.

The water annulus model has a shorter fuel cycle length compared to the solid reference pin model. Based on these facts and the physical design aspects of the water annulus fuel pin, this model was not considered further for coupling.

The designed helium annulus fuel pin used SiC cladding, where the thermal conductivity with two different grain sizes were modelled. The two models were developed and coupled to evaluate the effect of this cladding material. Both claddings produced similar temperatures. The helium annulus model, when compared to the solid reference model, performs better in terms of burnup, cycle length and has reduced maximum fuel temperatures during normal operating conditions.

The study succeeded in designing helium annulus fuel without altering the assembly dimensions and flow rates. This fuel pin design in a full core can be further investigated and tested under transient operating conditions.

**Keywords:** Solid reference fuel pin, water annulus pin, Helium annulus pin, Serpent 2.1.0, coupling

# ACKNOWLEDGEMENTS

I am deeply indebted to the National Nuclear Regulator of South Africa for awarding me the bursary to further my studies. Words cannot express my gratitude to my supervisor Prof Marina du Toit, and co-supervisor, Prof Frik van Niekerk, who generously provided time, knowledge and expertise. This endeavour would not have been possible without their great support.

I am also grateful to my friends and fellow NNR bursars for their editing help, feedback sessions and moral support. I am also thankful to my parents and siblings for their prayers and guidance.

Lastly, I am thankful to my spouse Emmanuel Moeketsi and daughter Olerato Moeketsi for their patience, love and understanding. They have kept my spirit and motivation high during this process.

I am infinitely grateful to God for His infinite grace, mercy, and provision.

# TABLE OF CONTENTS

# ABBREVIATIONS

| | |
|---|---|
| **3D** | Three-Dimensional |
| **ATF** | Accident Tolerant Fuels |
| **BOL** | Beginning Of Life |
| **CFD** | Computational Fluid Dynamics |
| **CHF** | Critical Heat Flux |
| **CVI** | Chemical Vapor Infiltration |
| **DBNR** | Departure from Nucleate Boiling Ratio |
| **DHS** | Distribution Heat Source |
| **EFPD** | Effective Full Power Days |
| **EOL** | End Of Life |
| **FA** | Fuel Assembly |
| **FCT** | Fuel Centreline Temperature |
| **FP** | Fission Product |
| **H/HM** | Hydrogen to Heavy Metal Ratio |
| **HPC** | High-Performance Computer |
| **IEA** | International Energy Agency |
| **INES** | International Nuclear and Radiological Event Scale |
| **IPCM** | Implicit Pressure Correction Method |
| **IRP** | Integrated Resource Plan |
| **LOCA** | Loss of Coolant Accident |
| **LWR** | Light Water Reactor |
| **MCNP** | Monte Carlo N-Particle Transport code 6 |
| **MFR** | Moderator to Fuel Ratio |
| **MIT** | Massachusetts Institute of Technology |
| **NEA** | Nuclear Energy Agency |
| **pcm** | per cent mille |
| **PLS** | Proportional Limit Strength |
| **PWR** | Pressurized Water Reactor |
| **RELAP** | Reactor Excursion and Leak Analysis Program |
| **SCWR** | Supercritical Water Reactor |
| **SiC** | Silicon Carbide |
| **$UO_2$** | Uranium Dioxide |
| **VIPRE-01** | Versatile Internals and Component Program for Reactors |
| **wt** | Weight |
| **λ** | Relaxation Factor |
| $k_{eff}$ | Effective Multiplication Factor |

# LIST OF TABLES

# LIST OF FIGURES

# CHAPTER 1

# INTRODUCTION

## Overview

Chapter 1 presents the conceptual basis of the study, which includes the research problem and purpose, aim, objectives, research method overview, and provisional chapter division.

## 1.1 Introduction

South Africa is a democratic republic with a population of 58.6 million and approximately 16.7 million households. Seventy-seven percent of the households are electrified, and 6 million remain without electricity (13.65% of the 6 million are primarily poor rural households) (Nuclear Power South Africa, 2021; Statistics South Africa, 2021). South Africa's power utility Eskom continues to implement loadshedding as the supply cannot cope with the increasing demand. As a democratic country, the right to access electricity for many poor South Africans is still not met.

In South Africa, coal is the primary energy source comprising around 80% of the country's energy mix. Coal is the largest source of global energy-related carbon emissions, which contributes to global warming. According to the International Atomic Energy Agency (IAEA), coal power needs to be reduced by 80% by 2030 to keep the world on track to meet the net-zero emissions target by 2050. South Africa's coal power should be reduced by 14% yearly (IEA, 2021).

According to the 2019 Integrated Resource Plan (IRP), by the year 2022, about 5400 MW of coal-fired power plants operated by Eskom will be decommissioned, increasing to 10500 MW by the year 2030 and 35000 MW by the year 2050. Reducing energy supply from obsolete coal-fired power plants and economic growth, spurring new energy demands, supports the provision of additional capacity from clean energy technologies, including nuclear. The IRP proposes that the nuclear power program be extended to 2500 MW and implemented reasonably and modularly (IRP, 2019).

The Koeberg nuclear power plant operates with two Pressurized Water Reactor (PWR) units, each with a 930 MWe net capacity. Koeberg supplies approximately 50% of the electricity demand of the Western Cape and contributes 5% to South Africa's total electricity needs (Nuclear Power South Africa, 2021). Most nuclear reactors worldwide are Light Water Reactors (LWRs). For many years, research on this type of reactor has been focussed on increasing power output and

minimizing nuclear waste. The focus recently shifted to the design of accident tolerant fuels after the catastrophic accident at Fukushima.

The Fukushima Daiichi nuclear power plant accident, initiated by the Tōhoku earthquake and tsunami on the 11th of March 2011, is categorized as a Loss of Coolant Accident (LOCA). The reactor core melted due to insufficient cooling, resulting in hydrogen gas formation in the containment. Hydrogen gas is formed when Zirconium alloy cladding reacts with water at elevated temperatures. Hydrogen gas mixed with oxygen in the containment resulted in an explosion, and radioactivity was released into the environment. The safety performance of LWRs in beyond-design basis accidents like Fukushima became a matter of grave concern and led to the development of the ATF concept (Koo *et al.*, 2014; Terrani, 2018; Otto *et al.*, 2014)

## 1.2 Research problem, Research purpose, and Objectives

### 1.2.1 Research problem

The Fukushima Daiichi nuclear accident is one of the two level-7 accidents on the International Nuclear and Radiological Event Scale (INES) of reactor accidents in the history of nuclear power. The belief was that all the backup electric power on-site and off-site was sufficient and that there would never be a loss of power with any significant safety implications contributed to the accident. The design of the Fukushima nuclear plant provided three primary levels of defence. The three primary levels of defence: (1) Plant equipment meant to provide reliable normal operation; (2) The equipment is intended to restore the plant to a safe state following an abnormal incident; (3) The safety systems designed to manage accident conditions. The design did not make sufficient provision for external hazards such as tsunamis.

Three levels of defence in depth were simultaneously challenged by the tsunami, resulting in failures of the backup diesel generators (IAEA, 2015). The first level of defence in depth in the nuclear reactor must start with the fuel pins, using fuel that can withstand heat for a while during design accidents. As a result, improving fuel limitations as the first line of defence is essential to prevent future catastrophic accidents.

### 1.2.2 Research purpose

The accident tolerance of nuclear fuel in nuclear reactors is a significant concern, as witnessed during the events at Fukushima. In the event of electricity loss, nuclear reactors depend on backup systems for cooling. When the backup system fails, a loss of coolant scenario could potentially occur, meaning insufficient heat is removed from the fuel element. The fuel element

may heat up beyond design limits which will cause fuel damage and, in severe cases, may lead to fuel element melting. The rationale behind ATF is to develop fuel that can withstand harsher conditions for longer times and, if not avoid imminent fuel damage following an initiating event, to at least provide a longer grace time to allow human intervention to mitigate or circumvent a looming catastrophic event.

The study aims to explore ATF characteristics and address safety considerations (such as, maximum fuel temperatures and hydrogen release) in LWRs during normal operation. Designing fuels that are accident tolerant should not only address the above issues but will also retain or improve the power output of nuclear reactors.

### 1.2.3 Objectives

The objectives of this study are:

- To evaluate proposed SiC cladded annular fuels in terms of neutronic and thermal-hydraulic characteristics and safety performance;
- To evaluate the optimal geometrical design parameters of SiC cladded annular fuel pin designs for a typical PWR for enhancing safety performance.
- To assess the potential for improving the safety of PWRs through SiC cladded annular fuels under normal conditions.

## 1.3 Research Methodology

The study proposes replacing Zirconium alloy with SiC and the solid-type fuel pellets with annular fuel. Serpent 2.1.0 (Leppänen, 2010) and Flownex 8.12.8 (Flownex SE, 2022) are used to model neutronics and thermal-hydraulics. The codes are coupled for iterative calculations to evaluate fuel safety characteristics.

The overall methodology used in the study consists of several stages:

- Collect data for the Koeberg PWR (or similar design North Anna),
- Collect data for suitable SiC material properties
- Collect data for various annular fuel dimensions and configurations
- Consider current and new annular fuel designs and introduce SiC cladding.
- Model the current Koeberg PWR (or similar, North Anna PWR) fuel pin and assembly in 3D.
- Model burnup for the fuel pin and assembly
- Model the proposed SiC cladded annular fuel pin and fuel assembly in 3D,

- Model burnup for the proposed SiC cladded annular fuel pin and assembly.
- Couple the neutronic and thermal-hydraulic models by creating the geometry and setting boundary conditions.
- Evaluate and present results and make further recommendations.
- The scope of this study is limited to a single pin coupled neutronic – burnup calculation for a representative fuel assembly. Full core cycle analysis is beyond the scope of this work.

## 1.4 Dissertation layout

The dissertation consists of the following chapters:

This current chapter provides background and motivation for the study. Chapter 2 presents a literature review on ATFs and materials' properties and discusses the relation between fuel centreline and maximum fuel temperatures.

Chapter 3 explains some of the essential neutronic parameters investigated in the study. Furthermore, it explains validation and verification, which are essential for modelling. Chapter 4 provides a detailed methodology and verification applied to all the models in the study. In Chapter 5 analyses of results and conclusions are presented, and recommendations for future studies are made.

# CHAPTER 2

# LITERATURE REVIEW

### Overview

A literature review on ATFs and the properties of materials used in the study is covered in Chapter 2.

## 2.1 ATF

ATF is a term used to describe a series of new nuclear fuel concepts, including different fuel pins, cladding materials, and fuel pellet designs, that can improve the fuel performance of LWRs during normal operations, transient conditions, and accident scenarios. Nuclear reactors operate at high temperatures, which expose fuel inside the reactor core to harsh conditions. ATFs are developed to render improved tolerance to accident scenarios, including being more resistant to higher temperatures (e.g., providing higher melting points and better thermal conductivity to enhance heat removal), as stipulated in Figure 2-1.

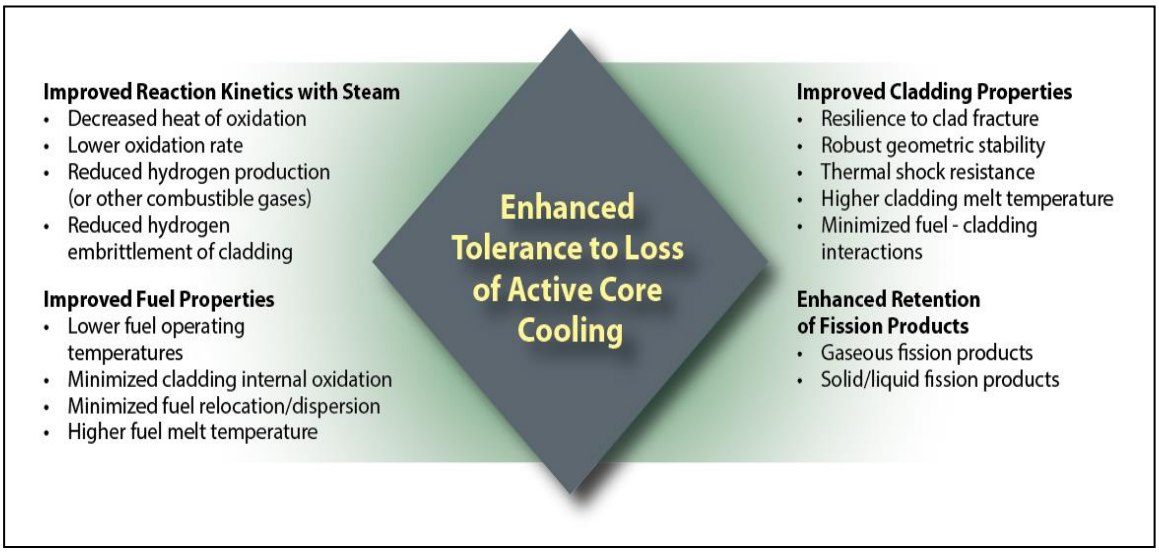


**Figure 2-1: Description of ATF (Carmack, 2016)**

ATF uses new materials that reduce or eliminate hydrogen build-up, enhance fission product retention, and are more structurally resistant to radiation, corrosion, and high temperatures during accidents (Dobisesky et al., 2014). In short, ATF research aims to limit or circumvent fuel damage

(often resulting in increased grace time) in an accident scenario associated with loss of coolant. Figure 2-2 illustrates different categories of ATF.

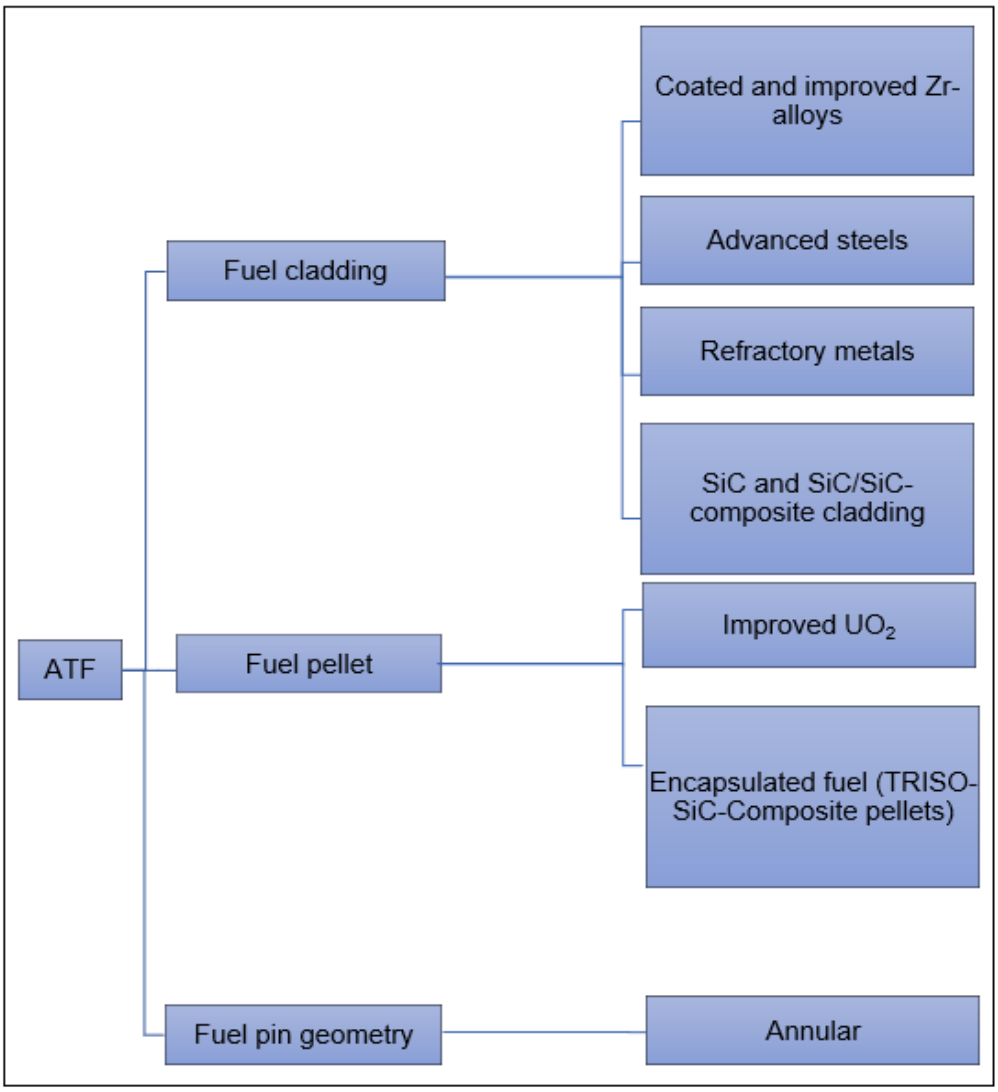


**Figure 2-2: Types of ATF**

Advanced fuel cladding materials include coated and improved Zirconium alloys and Silicon Carbide (SiC) composite. Advanced fuel pellet designs focus on improved fuel pellets such as encapsulated pellets (e.g., TRISO-SiC-composite pellets, which are kernels coated with multi-layers of carbon and SiC and different fuel pin geometries, e.g., annular fuel concepts).

## 2.2 Fuel cladding

### 2.2.1 Zircaloy-4

#### 2.2.1.1 Material properties

Zirconium is a transition metal used in a solution with other metals to form Zirconium alloys. Zircaloy-4 is one of the zirconium alloys mainly used in nuclear technology as fuel rod cladding. For this study Zircalot-4 is used as cladding due to the availability of information. However, there are more advanced Zirconium alloys in existence that have been used in PWRs more recently.

**Table 2-1: Physical, mechanical, and thermal properties of SiC and Zircaloy-4 (ATI Metals, 2015; Li, 2013; Nuclear power, 2022e)**

| Properties | Zircaloy-4 | SiC | Units (SI) |
|---|---|---|---|
| Density | 6.55 | 3.21 | $g/cm^3$ |
| Melting Temperature | 2128 | 3000 | K |
| Thermal Conductivity | 23 | 350 | W/mK |
| Shear Modulus | 36.2 | 32 - 51 | GPa |
| Tensile Strength | 514 | 240 - 1625 | MPa |
| Poisson's Ratio | 0.41 | 0.21 | - |
| Specific Heat | 270 | 510 - 650 | J/kg.K |
| Young's Modulus | 99.3 | 90 - 137 | GPa |
| Resistivity | 7.4x10^-7 | 41.7– 202 (x10^-8) | Ohm.m |
| Thermal neutron absorption cross-section | 0.18x10^-28 | 0.12x10^-28 | $m^2$ |

#### 2.2.1.2 Advantages

Zirconium has a high thermal neutron absorption cross-section, as seen in Table 2-1. Zirconium alloy has exceptional corrosion resistance to various acids (such as nitric acid, acetic acid, sulfuric acid, and hydrochloric acid), salts, and alkalis. Zirconium resists corrosion well in high-temperature and high-pressure water conditions.

#### 2.2.1.3 Disadvantages

Zirconium alloys are easily welded/sealed, but as with all reactive metals, great care must be taken to avoid picking up interstitial components like oxygen, carbon, and nitrogen that could

compromise the weld's mechanical characteristics and corrosion performance (Young *et al.*, 2012).

Zirconium alloys have low strength and heat resistance. At high temperatures, they are oxidized by steam and other gases via the reaction in Equation 2-1. The reaction is exothermic and causes the mechanical properties to degrade while also releasing heat and hydrogen. The reaction is substantially more intense and hazardous for nuclear power plant safety during accidents like LOCA (Nuclear power, 2021).

$$Z_r + 2H_2O \rightarrow Z_rO_2 + 2H_2 \qquad 2\text{-}1$$

### 2.2.2 SiC

#### 2.2.2.1 Material properties

SiC has exceptional thermal properties, high thermal conductivity, and low thermal expansion. SiC has a smaller neutron absorption cross section than Zirconium, among other things, due to its density being half that of Zirconium, as shown in Table 2-1. SiC is less susceptible to degrading chemical interactions, stable under irradiation and does not creep below 1000°C (Carpenter, 2006). The SiC cladding concept has several variants: full composite cladding, a composite layer, and a monolithic ceramic layer which can be placed on the inside or outside of the fuel rod (Singh *et al.*, 2018). The SiC composite cladding increases maximum tolerable cladding temperatures from the current 2128 to 3000 K and increases corrosion resistance under normal operating conditions (IAEA, 2014).

Fuel cladding thermal conductivity is crucial as it affects the temperature of the cladding and that of the fuel. A higher thermal conductivity will decrease the cladding and average fuel temperatures. Thermal conductivity also depends on grain size.

Figure 2-3 shows the thermal conductivity of SiC at elevated temperatures and different grain sizes (Li, 2013).

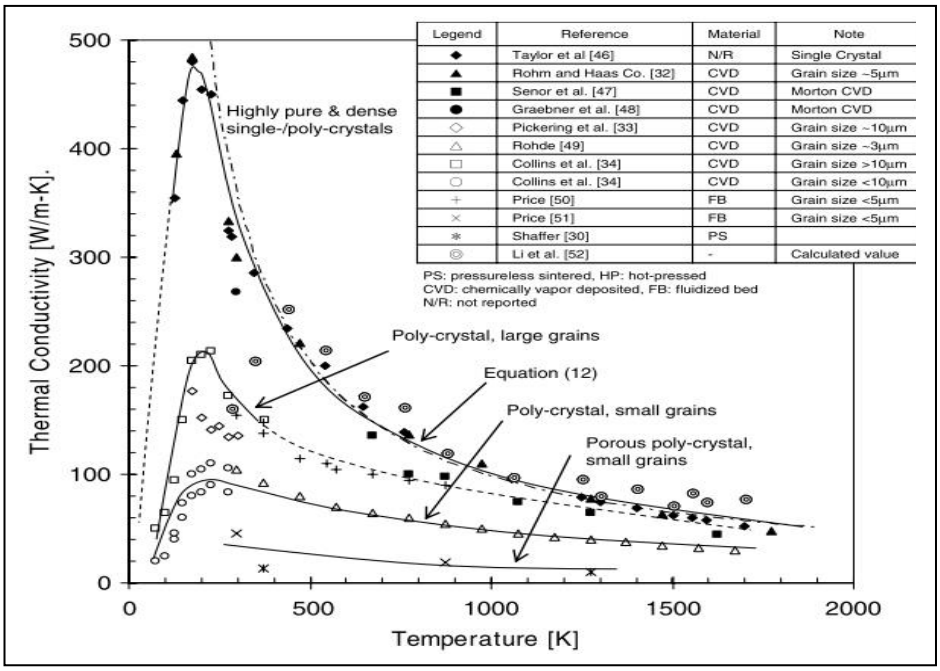


**Figure 2-3: Thermal conductivity of SiC at elevated temperatures (Li, 2013)**

#### 2.2.2.2 Advantages

Adding SiC as fuel cladding to $UO_2$ fuel will improve the fuel's thermal conductivity while preserving some critical $UO_2$ features, such as the high melting point. SiC cladding can achieve high thermal conductivity of 350 W/mK, as shown in Table 2-1. $UO_2$ has a thermal conductivity of 23 W/mK; thus, adding SiC to the fuel cladding can significantly increase its thermal conductivity (Abdalla, 2012). Due to the higher thermal conductivity, the fuel enrichment in fuel pins with SiC cladding can be lowered, or the enrichment can be kept unchanged while the burnup is increased, which can significantly benefit fuel economy (Slabber, 2014).

SiC is compatible with $UO_2$ fuel, the most widely used fuel in nuclear power plants. The properties of SiC suggest that SiC cladding is far better than Zircaloy cladding.

#### 2.2.2.3 Disadvantages

SiC has a hardness of 2800 Kg/mm$^2$, with carbon bonds held together by covalent bonds that are not easily broken, which makes it challenging to join/seal SiC cladding materials together. Numerous joining techniques/methods have been tested, for instance, Chemical Vapor Infiltration (CVI), used to prepare fiber-reinforced SiC ceramic matrix composites ($SiC_f$/ SiC).

SiC-based materials undergo hydrothermal corrosion. The corrosion process begins when Si in SiC oxidises to form silica, and the C in SiC forms volatilises such as $CO_2$, CO, or $CH_4$, depending on the activity of oxygen in the system (Terrani *et al.*, 2015). However, silica dissolves fast in aqueous environments as silicic acid because silica is abundantly soluble in high-temperature water. The dissolution rate of silica is substantially faster than the rate of silica production. The rate of silica formation is slow because the dissolved hydrogen lowers oxygen activity and the redox potential in the system (Terrani, 2018).

Yueh and Terrani also identified one of the disadvantages of SiC through experiments: when silicon oxidises, it releases silica into the nuclear reactor coolant, which is concerning as the current nuclear plant systems have limited ability to remove silicon (Yueh and Terrani, 2014). Silica oxidises according to Equations 2-2, 2-3, and 2-4 (Rebak, 2020).

$$\boldsymbol{SiC + 2H_2O \rightarrow SiO_2 + CH_4} \quad \text{2-2}$$

$$\boldsymbol{SiC + 3H_2O \rightarrow SiO_2 + 3H_2 + CO} \quad \text{2-3}$$

$$\boldsymbol{SiC + 4H_2O \rightarrow SiO_2 + 4H_2 + CO_2} \quad \text{2-4}$$

SiC/SiC fuel cladding has the potential to fail due to microcracking. The formation of a microcracks pathway network allows radionuclides to escape from the internal cladding to the coolant. Failure in SiC/SiC composites may occur at an ultimate tensile stress of ~200 - ~400 MPa and a strain of ~0.5%. Microcracking develops when the Proportional Limit Strength (PLS) manifests at ~90 MPa (CVI) to ~200 MPa or when a strain of ~0.05% is reached (Terrani, 2018). The ultimate strength of SiC is lower than that of Zircaloy-4 with 514 MPa, however the high thermal conductivity of SiC is an advantage (Nuclear power, 2022g).

## 2.3 Fuel pins

The are different types of nuclear fuel pins for LWRs. The solid fuel pin is the most used, and an alternative fuel pellet design is called the annular fuel pin, depicted in Figure 2-4 for a solid fuel pin on the left, where the fuel pellet is the yellow circle in the centre and an annular pin on the right. The blue circle in the centre represents water for the annular fuel pin. Helium is used to pressurize all fuel rods during fabrication to reduce stress and strain during in-core operation; helium is depicted in white.

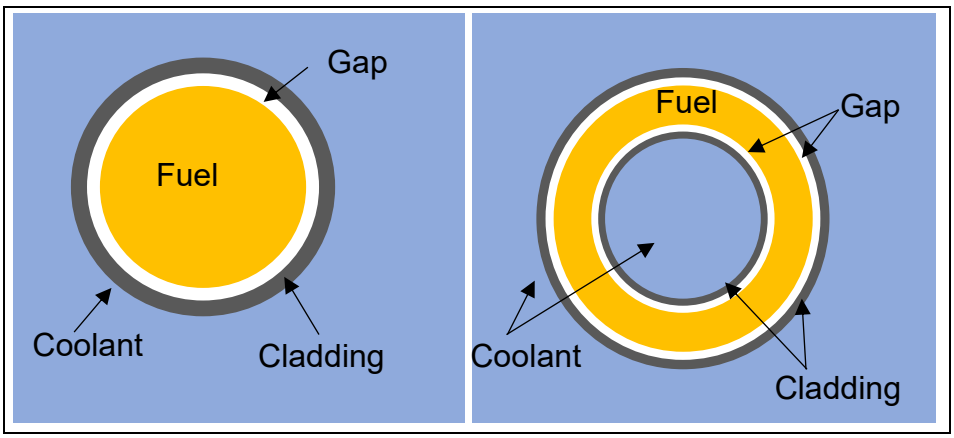


**Figure 2-4: Solid fuel pin (Left) and an internal and external water-cooled annular fuel pin (right)** (Pane *et al.*, 2018)

### 2.3.1 Annular fuel pin

The Massachusetts Institute of Technology (MIT) proposed annular fuel for PWRs to alleviate the problem of central heat accumulation in solid fuel pins. Annular fuel pins provide internal and external cooling, using water as the coolant (Hejzlar and Kazimi, 2008). The diameter of annular fuel rods is significantly larger than the standard solid fuel pins to accommodate an inner coolant channel that allows for adequate coolant flow. The number of fuel pins in an annular fuel assembly will be significantly smaller than the conventional 17x17 array for solid fuel pins for a fixed fuel assembly size. The energy generated within a solid fuel pin is transferred to the external coolant through the cladding (Feng *et al.*, 2017). However, the energy generated in annular fuel rods is transferred to the internal and external cooling surfaces through the cladding (Kianpour *et al.*, 2020).

#### 2.3.1.1 Geometry

Numerous studies of annular fuels have been published in the literature, listed in Table 2-2, and each used different fuel pin dimensions and assembly arrays (Ufsar, 2009; Horelik *et al.*, 2018). Different fuel assembly arrays and pin dimensions with calculated H/HM ratios are summarised in Table 2-3. Fuel assembly dimensions and H/HM ratios are summarised in Table 2-4. The units used for the dimensions in Table 2-3 and Table 2-4 are cm, where A designates the area, and R is the radius. The subscripts ci, f, and co designate inner cladding, fuel, and outer cladding; the second subscript designates the outer (o) or inner (i) surface.

**Table 2-2: Different work done on annular fuels**

| Reference | Fuel assembly array | |
|---|---|---|
| | **Solid fuel** | **Annular fuel** |
| (Feng *et al.*, 2017) | 17x17 | 15x15 |
| | | 14x14 |
| | | 13x13 |
| | | 12x12 |
| | | 11x11 |
| (Silva *et al.*, 2017) | 16x16 | 15x15 |
| | | 14x14 |
| | | 13x13 |
| (Hejzlar and Kazimi, 2007) | 17x17 | 13x13 |
| | | 12x12 |
| (El-Sahlamy *et al.*, 2020) | 17x17 | 13x13 |
| (Deng *et al.*, 2020) | - | 13x13 |
| (Ellis, 2006) | 17x17 | 13x13 |
| (Pane *et al.*, 2018) | 17x17 | 13x13 |

**Table 2-3: Annular fuel pin dimensions and H/HM ratio for different arrays**

| Array | Dcii | Dcio | Dfi | Dfo | Dci | Dco | Pitch | H/HM pin |
|---|---|---|---|---|---|---|---|---|
| **11x11** | 1.0733 | 1.1876 | 1.2000 | 1.7000 | 1.7124 | 1.8267 | 1.9520 | 7.8036 |
| **12x12** | 0.9533 | 1.0676 | 1.0800 | 1.5400 | 1.5524 | 1.6667 | 1.7890 | 7.6733 |
| **13x13** | 0.8633 | 0.9776 | 0.9900 | 1.4100 | 1.4224 | 1.5367 | 1.6510 | 7.6729 |
| **14x14** | 0.7533 | 0.8676 | 0.8800 | 1.2940 | 1.3064 | 1.4207 | 1.5330 | 6.9887 |
| **15x15** | 0.6733 | 0.7876 | 0.8000 | 1.1978 | 1.2102 | 1.3245 | 1.4310 | 6.6211 |

**Table 2-4: Annular fuel assembly dimensions and H/HM ratio for different arrays**

| Array | No. Guide tubes | No. fuel pins | R in guide | R out guide | Pitch | H/HM Assembly |
|---|---|---|---|---|---|---|
| **11x11** | 7 | 114 | 0.5715 | 0.6121 | 21.4720 | 8.34424 |
| **12x12** | 8 | 136 | 0.5715 | 0.6121 | 21.4680 | 8.19391 |
| **13x13** | 9 | 160 | 0.5715 | 0.6121 | 21.4630 | 8.20496 |
| **14x14** | 12 | 184 | 0.5715 | 0.6121 | 19.8898 | 7.54258 |
| **15x15** | 20 | 205 | 0.5715 | 0.6121 | 19.8675 | 7.40671 |

On a unit cell basis, the annular fuel lattice with a 13x13 array has a 10% higher water-to-fuel ratio than the conventional solid fuel pin. As a result of the improved moderation, the eigenvalue increases (Kazimi and Hejzlar, 2006).

#### 2.3.1.2 Advantages

The fuel thickness in an annular fuel pellet is reduced; thus, the peak temperature is decreased. Annular fuel assemblies can endure substantial power upgrades while maintaining sufficient Departure from Nucleate Boiling Ratio safety margin (DNBR) (Ansarifar *et al.*, 2016).

The centreline temperature is lower for annular fuel pins with internal and external cooling than for ordinary solid fuel pins. Peak temperature in an annular fuel pin can be significantly reduced since fuel thickness is reduced and heat is removed from both sides. The annular fuel pin's characteristics will increase safety margins for various transients and accidents (Mozafari and Faghihi, 2013).

#### 2.3.1.3 Disadvantages

Internally and externally cooled annular fuels with Zirconium cladding bring a much higher Zircaloy charge in the reactor core, which can increase hydrogen formation (with associated risks) in severe accidents. It is vital to consider alternative fuel cladding for dual-cooled annular fuels (Deng *et al.*, 2021).

### 2.3.2 TRISO-SiC composite pellets

Encapsulated fuel TRISO-SiC-composite pellets are a kind of micro fuel particle that comprises fissile material-bearing kernels of $UO_2$ that are covered within several layers of carbon and a layer of SiC, as seen in Figure 2-5 (Jiang *et al.*, 2021). Each particle acts as its containment system

because of its triple-covered layers. These layers retain fission products under normal, transient, and accident reactor operating conditions.

TRISO particles can withstand extreme temperatures exceeding the limit of current nuclear fuels. The TRISO-SiC fuel is envisioned as a viable medium-term replacement for present $UO_2$ fuel pellets. Potentially, it has enhanced safety qualities than alternative fuel types, owing to its many barriers to Fission Product (FP) dispersion, solid mechanical stability, and good thermal conductivity (Nuclear power, 2021). TRISO-SiC particles are outside the scope of this study, but they can potentially be investigated in future studies.

**Figure 2-5: TRISO-SiC-composite pellets (Nuclear power, 2021)**

## 2.4 Fuel Centreline Temperature (FCT)

$UO_2$ fuel pellets are compressed and sintered into a solid, subsequently loaded and enclosed within fuel rods with Zirconium alloy or SiC cladding. Nuclear fuel is subjected to hostile conditions inside the nuclear reactor. Correctly determining the precise temperature distribution in each fuel rod is essential to monitor fuel elements close to or beyond melting points which may cause thermal damage. The fuel pin centreline presents the origin for r-coordinates where $r = 0$; thus, the temperature in a fuel pin is solved as a function of radius T(r) (Yapici, 2002).

$$\frac{1}{r}\frac{d}{dr}\left(r\frac{dT}{dr}\right)+\frac{qv}{k}=0 \qquad 2\text{-}5$$

where $k$ is the thermal conductivity (W/m.K), and $qv$ is the rate of energy production per unit volume.

$$r\frac{dT}{dr}=-\frac{qv}{2k}r^2+C_1 \qquad 2\text{-}6$$

$$T(r)=-\frac{qv}{4k}r^2+C_1 lnr+C_2 \qquad 2\text{-}7$$

where $C_1$ and $C_2$ are integration constants.

The cylindrical heat Equation 2-5 is solved by the separation of variables method to obtain Equations 2-6 and 2-7. These equations calculate the temperature distribution in the fuel pin when the thermal conductivity is constant. Fuel centreline temperature is identified as the point $T_m$ in Figure 2-6, which is a point where the temperature is maximum. The fuel centreline temperature at point $T_m$ can reach over 1273.1 °C at the boundary conditions stipulated in Equations 2-8 and 2-9, where $C_1 = 0$ (Nuclear power, 2022d).

$$C_2=T_U+\frac{qv}{4k}r_U^2 \qquad 2\text{-}8$$

$$T(0)=\frac{qv}{4k}r_U^2\left(1-\frac{r^2}{r_U^2}\right)+T_U=1273\ ℃ \qquad 2\text{-}9$$

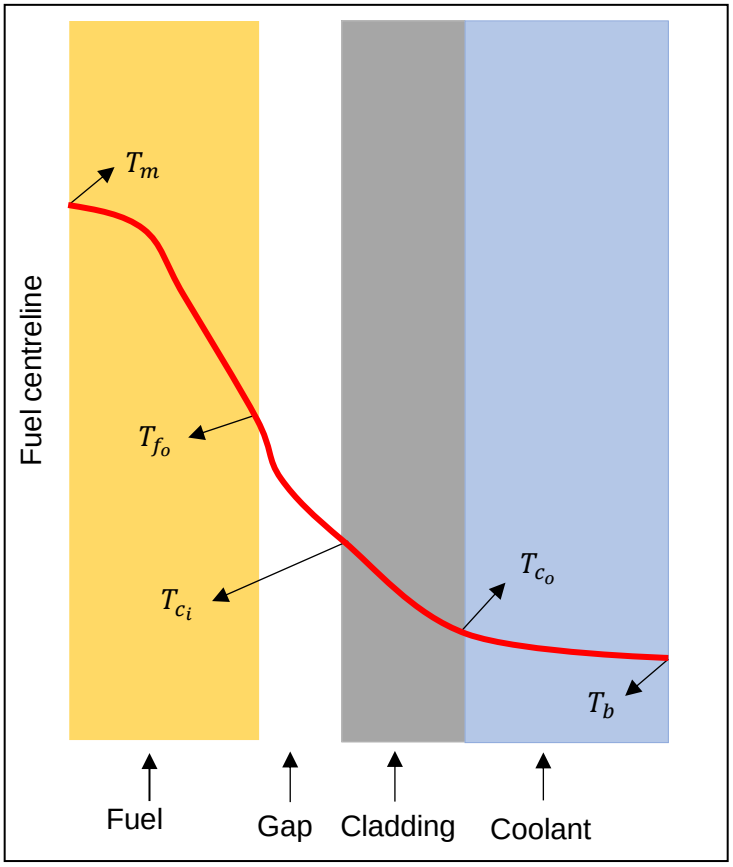


**Figure 2-6: Solid fuel pin temperature profile (Allison, 2013)**

In Figure 2-6, $T$ designates temperature, $m$ is for maximum and $b$ stands for bulk. The subscripts $c_i$, $c_o$, and $f_o$ designate inner cladding, outer cladding, and outer fuel.

## 2.5 Maximum fuel temperature

Annular fuels have a gap in the middle; therefore, the maximum fuel temperature is at the point $T_{f_i}$ in Figure 2-7. Equation 2-10 is solved to determine the maximum fuel temperature at point $T_{f_i}$.

$$\frac{1}{r}\frac{d}{dr}\left(k_f(T)r\frac{dT}{dr}\right) + Q_p = 0 \qquad 2\text{-}10$$

Where $k_f$ is the fuel's thermal conductivity and $Q_p$ is the power density.

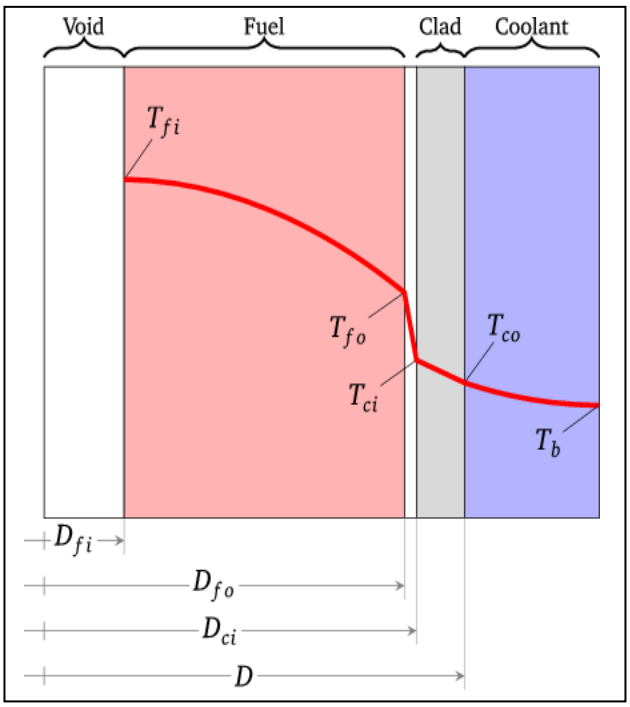


**Figure 2-7: Helium annular fuel pin temperature profile (Lodi *et al.*, 2016)**

Figure 2-7 depicts a helium annulus fuel pin with external fuel cladding only. The fuel cladding has two diameters, the inner ($D_{ci}$) and the outer ($D$). Temperature was evaluated for the cladding at the inner cladding ($T_{ci}$ is temperature of the inner diameter of the external cladding) and outer cladding ($T_{co}$ is the temperature of the outer diameter of the external cladding) respectively. Dimensions units in cm, $b$ stands for bulk. The subscripts $f_i$ and $f_o$ designate inner fuel, and outer fuel. Figure 2-7 is an example of helium annulus fuel pin temperature profile. It must be noted that the water annulus fuel pin has internal and external fuel cladding. Where, the water inside the fuel pin passes through the internal cladding.

Three studies were done on the solid and water annular fuel pin models. The maximum fuel temperatures reported in the three studies are listed in Table 2-5. The two reference studies used the same fuel pin dimensions.

**Table 2-5: Maximum fuel temperature for solid and water annular fuel**

| Reference | Solid fuel | Annular fuel | Unit |
|---|---|---|---|
| | 17x17 | 13x13 | |
| (El-Sahlamy *et al.*, 2020) | 2476.15 | 904.15[1] | K |
| (Hejzlar and Kazimi, 2007) | 2573.15 | 1073.15[2] | K |
| (Kazimi and Hejzlar, 2006) | 2573.15 | 1018.15[3] | K |

## 2.6 Adaptive relaxation in coupling

The distribution of the core power and the moderation are both affected by the change in coolant density. Coupling the neutronic and thermal-hydraulic models is essential to accurately simulate the change in the coolant density and temperature during steady state analysis (Wang *et al.*, 2017). An iterative process is used between the neutronic and thermal-hydraulic codes to achieve convergence in power distribution. The relaxation factor (λ) is introduced in the neutronic code to relax the power. The purpose of this iteration is for the power distribution to converge. λ aims to reduce the difference between iterations and prevent divergence from abrupt change and significant power difference. The successive iteration method uses the same λ from the initial power distribution until convergence. However, the process requires too many iterations. In contrast, the adaptive iterative method uses a different λ every iteration to accelerate convergence (Liu and Cai, 2013).

Liu and Cai attempted to select the maximum λ through calculations. Using averaged initial power distribution, they changed λ to 0.5, 0.2, and 0.1 and compared the maximum relative deviation during iteration. When λ decreases, the minimum and maximum oscillating deviation get less. When λ is decreased to 0.1, it stops oscillating and converges. The maximum λ is 0.18, where λ is gradually adapted until convergence. Another approach was to set the initial power distribution as sinusoidal distribution, where they compared the maximum relative deviation of 0.15 and 0.18. in this case, the maximum λ for the sinusoidal distribution is not 0.18 but 0.15, which makes it hard to select one λ factor (Liu and Cai, 2013). The λ can be changed gradually from iteration to iteration to reach convergence faster.

[1] El-Sahlamy *et al.*, used MCNP6 and RELAP5 codes with fuel enrichment of 4.95 wt%. ENDF/B-VII.1 libraries used. MCNP6 can model annular fuel rods.

[2] Hejzlar and Kazimi, used Versatile Internals and Component Program for Reactors (VIPRE-01) and RELAP3D codes with fuel enrichemnt 5 wt%. VIPRE-01 does not provide an option for fuel rods with internal cooling, the annular fuel rods were specified as heat-generating tubes with five material regions.

[3] The flow rate used in all three studies is not the same and the modelling methods.

## 2.7 Conclusion

To better grasp the following chapters, Chapter 2 provided some background on different types of ATFs, their advantages, and disadvantages. The solid fuel pin temperature, called centreline temperature, and the annular fuel temperature, called maximum temperature, are presented as thermal-hydraulic parameters. The coupling method of adaptive relaxation is introduced. Based on the investigated ATF concepts, annular fuel geometry was chosen together with the addition of SiC as cladding. Internally and externally cooled annular fuel has been extensively investigated; however, the drawback of this fuel is the higher captures in the cladding, more expensive and complex manufacturing, and the issue of ensuring flow through the internal annulus. This study will therefore aim to modify the internally and externally cooled annular fuel by removing the water annulus on the inside, thereby removing the inner cladding layer. The inner cladding and the water annulus are replaced with a void, with only the outer cladding remaining as the fission barrier.

# CHAPTER 3

# THEORY

### Overview

This chapter presents the theoretical background on neutronic parameters such as reactivity and Shannon entropy and highlights the importance of these parameters.

## 3.1 Neutronic parameters

### 3.1.1 Effective multiplication factor ($k_{eff}$)

The fission neutron population changes from one generation to the next and is measured by the effective multiplication factor.

If:

- $k_{eff}$ = 1 Critical (neutron population in the assembly remains constant, self-sustained reaction), the reactor operates at a constant power.
- $k_{eff}$ > 1 Supercritical (neutron production is greater than the absorption and leakage), the reactor power levels are rising.
- $k_{eff}$ < 1 Subcritical (neutron production is less than the absorption and leakage), the reactor power levels are decreasing.

Factors that affect $k_{eff}$.

If $k_{eff}$>1, the following factors will help reduce it.

- Control rod - inserting the control rod, adding new absorbing material, thus decreasing thermal utilization.
- Boron – Boric acid diluted in the primary coolant causes new absorbing material; thus, thermal utilisation decreases.
- Change in moderator temperature/ Fuel temperature.
- The presence of burnable absorbers in the fuel, adding burnable absorbers causes a decrease in the thermal utilisation factor.

### 3.1.2 Reactivity ($\rho$)

Reactivity is the fractional change in neutron population per generation (a measure of a reactor's departure from criticality). The reactivity is zero for critical conditions. The larger the absolute value of reactivity in the reactor core, the further the reactor is from criticality. Equation 3-1 is used to determine the reactivity from $k_{eff}$ (Lamarsh and Baratta, 2001; Nuclear power, 2022c).

$$\boldsymbol{\rho = \frac{k_{eff} - 1}{k_{eff}}} \qquad 3\text{-}1$$

where $\rho$ is the reactivity and $k_{eff}$ is the effective multiplication factor.

### 3.1.3 Shannon entropy

In Monte Carlo k-eigenvalue calculations, the Shannon entropy is frequently used to assess the convergence of the fission source. It is crucial to recognise when the iteration procedure has converged so that a significant number of the initial batches/cycles are deleted to receive accurate findings free of contamination from the original guess for the fission distribution. In the Serpent code, the Shannon entropy setting needs to be included for the code to calculate it. Shannon entropy is given by Equation 3-2 (Brown, 2006).

$$\boldsymbol{H_{src} = -\sum_{J=1}^{N} P_J . ln_2(P_J)} \qquad 3\text{-}2$$

where $N$ is the number of grid boxes in the superimposed mesh and $P_J =$ (number of source sites in J-th grid box)/(total number of source sites).

### 3.1.4 Burnup

Fuel burnup or fuel utilisation is a nuclear engineering term that describes how much energy is extracted from nuclear fuel and how much fuel is depleted. The fission energy release per unit mass of fuel is generally expressed in Megawatt-days per Metric Ton of Uranium (MWd/MTU). Fuel burnup determines the amount of energy released and the isotopic composition of irradiated fuel (Nuclear power, 2022a).

### 3.1.5 Atom density

Atom density is the number of atoms contained in 1 $cm^3$ of a substance. Isotope atom density is the total atom density of the element multiplied by the isotopic abundance. Equation 3-3 for the

isotope atom density is used to determine material compositions expressed in cubic (atoms/cm3) or (atom/barn cm). Atom density is a critical parameter contributing to the precision of neutronic calculations used in the reactor core design and core power distribution (Lamarsh and Baratta, 2001; Horelik *et al.*, 2018).

$$\boldsymbol{N_i = \frac{\gamma_i \rho N_A}{100M}} \qquad 3\text{-}3$$

Where:

$N_i$ is the atom density (atoms per cm$^3$),

$\gamma_i$ is the isotopic abundance in atom percent,

$M$ is the molar mass (g), $\rho$ is density (g/cm$^3$), and

$N_A$ is Avogadro's number, which is a constant (mol$^{-1}$).

## 3.2 Hydrogen to Heavy Metal ratio (H/HM)

The H/HM ratio influences the neutron spectrum, also called the Moderator to Fuel Ratio (MFR) or $V_m/V_f$. When the H/HM ratio increases, the system is over-moderated, favouring the fission reaction. In parallel, a reduced H/HM ratio will result in a system under moderated, favouring neutron capture in fertile materials (du Toit, 2017; Weaver and Herring, 2002).

$$\boldsymbol{\frac{H}{HM} = 2 \times \frac{M_{fuel}}{M_{H_2O}} \times \frac{\rho_{H_2O}}{\rho_{fuel}} \times \frac{V_{H_2O}}{V_{fuel}}} \qquad 3\text{-}4$$

$M$ is the atomic weight of the moderator or fuel, $\rho$ is the density of the moderator or the fuel, and $V$ is the volume that the fuel or moderator occupies.

Historically there has been a trend towards increasing H/HM (less fuel, more water) for the same fuel enrichment to gain greater economics through higher discharge burnup

In subsequent chapters, the H/HM ratio for the solid and the annular fuel pin models is calculated using Equation 3-4. To calculate the H/HM ratio for the solid and annular fuel assemblies, the water area in and around the fuel pins was calculated using Equation 3-5. The area occupied by $H_2O$ inside and outside the guide tube is determined and in Equation **3-5** the area accounts for both the water inside and outside the guide tube.

$$\boldsymbol{Area\ H_2O = (No.Guide\ tubes\ x\ Area\ H_2O\ \{out + in\}\ guide\ tubes) + (No.fuel\ cell\ x\ Area\ in\ H_2O\ in\ fuel\ cell)} \qquad 3\text{-}5$$

## 3.3 Self-shielding

There are two categories of self-shielding: energy self-shielding and spatial self-shielding. When calculating reaction rates, it is important to consider the self-shielding aspects, which is crucial because it affects numerous observables, such as criticality and activation.

Cross-sections frequently contain resonances established for specific energy regions and frequently contribute significantly to the overall reaction rate, and this is a crucial component of energy self-shielding. A neutron energy spectrum covers various materials' resonance regions in nuclear reactors, specifically thermal reactors. When the neutron energy is near resonances energies, the absorption probability of the neutron increases. Thus, the effective absorption of each nucleus is reduced due to the energy-dependent flux being depressed. When a neutron is below or above energy resonance, the neutron flux is almost the same. This neutron flux reduction near the resonance energy describes energy-shielding. A depressed energy-dependent flux of energy self-shielding is dramatic. Spatial self-shielding focuses on neutron flux and local spectra changes over short distances (Stacey, 2007; Lamarsh and Baratta, 2001; Nuclear power, 2022c).

In nuclear fuels, due to doppler broadening, the neutrons absorbed in the resonance region increase with increasing temperature. Thus, the average travel distance of neutrons between collisions decreases. Some neutrons entering the fuel region from the moderator region are absorbed in the outer surface of the fuel pellet. The neutron flux in the inner region of the fuel pellet is lower, as there is less fission compared to the outer regions (Beydoğan *et al.*, 2016). The scope of self-shielding is a study on its own, and it can be considered for annular fuels.

## 3.4 Validation and Verification

In the nuclear industry, computer modeling software codes simulate real nuclear reactors. Verification ensures a software accomplishes its objective within acceptable uncertainty and standards. On the other hand, validation is the process that involves determining whether the software products meet the requirements. It ensures that the system model sufficiently represents the physical system or design under consideration (Sargent, 2013). The validation and verification of the codes used for this study are discussed in Section 4.6.

## 3.5 Conclusion

Background information on a few of the significant neutronic parameters was provided in Chapter 3. Reactivity, burnup, and Shannon entropy are some of these parameters. This chapter describes how atom density is used to determine the composition of materials. Every study needs to be verified and validated; these concepts are also explained.

# CHAPTER 4

# METHODOLOGY

### Overview

In this chapter, the codes and tools used are explained beforehand. The North Anna PWR model is presented as the reference reactor used in the study to illustrate the neutronic and thermal-hydraulic modeling employed in the simulations. Two annular fuels are modelled: an existing dual-cooled fuel and a newly designed helium annular fuel. The modelling methodology utilised for these fuels is explained in detail. All the models in this chapter are validated and verified.

## 4.1 Codes and Tools

### 4.1.1 Serpent

Serpent is a Monte Carlo code under development since 2004 at VTT Technical Research Centre in Finland. It is a three-dimensional continuous-energy reactor physics burnup calculation code. Although the system is designed for lattice physics, the universe-based geometry description allows transport simulation in three-dimensional geometries (Leppänen *et al.*, 2014). Serpent has more potential in the field of radiation transport applications like decommissioning of reactors as well as spent fuel storage, transportation, and final disposal (Leppänen, 2010). Serpent can also perform coupled multi-physics applications and photon transport (such as coupled neutron–photon transport) (Kaltiaisenaho, 2020).

Serpent calculates burnup using self-contained built-in subroutines without relying on external depletion solvers. Calculating isotopic one-group transmutation cross-sections for each depleted material at each depletion phase is a cyclic procedure in fuel depletion simulation. This information is paired with fission yields and radioactive decay constants to produce a set of coupled first-order differential equations. Serpent includes ENDF format data libraries to read radioactive decay data, energy-dependent fission yields and isomeric branching ratios for neutron processes. During transport simulation, the one-group transmutation cross-sections are required to solve the Bateman depletion equations. To speed up the calculation for each burnable material after the simulation is completed, the continuous-energy cross-section with flux spectra is collapsed, and this method is known as spectrum-collapse (Leppänen *et al.*, 2014). Serpent is used in this study for neutronic and burnup calculations.

### 4.1.2 Flownex

Flownex is a dynamic Computational Fluid Dynamics (CFD) simulation code. This code enables users to analyse and construct complicated thermal-fluid systems and networks for power plants in detail. It uses an Implicit Pressure Correction Method (IPCM) to solve the momentum equation in each element and the energy and continuity equation at each node. Flownex can simulate steady-state and dynamic flows using the algorithm, which provides the code with pseudo CFD capabilities. This capability allows the prediction of complicated events like temperature and pressure waves in pipes and the effect of buoyancy in packed bed reactors.

The code has a solver feature that enables it to deal with steady-state and transient flows. Real-time simulations can be executed on basic desktop computers with fast simulation speeds. Numerous problems can be solved at the same time. In the nuclear industry, Flownex estimates heat transfer, mass flows, and pressure in the reactor core during normal operating and accident conditions (Van Ravenswaay *et al.*, 2006).

The Distribution Heat Source (DHS) element in Flownex simulates the creation of heat in materials. The overall heat fraction, the heat fraction of the flow, and the heat of the layers in the direction of heat transfer are the three heat fraction options for heat distribution within the DHS (Flownex SE, 2022). Due to Flownex's ability to model coolant density and temperature, as well as fuel temperatures, it is utilised in this study for the thermal-hydraulic calculation.

### 4.1.3 Coupling

The coolant's thermal-hydraulic parameters substantially influence nuclear reactors' neutron spectrum and power distribution. The neutronic code determines the neutron spectrum and power, and the thermal-hydraulic code estimates the coolant parameters such as density and temperature (Safavi *et al.*, 2020). Coupling is the process of combining neutronic and thermal-hydraulic codes. Coupling can be internal or external. In internal coupling, two codes are integrated, and the data transfer occurs within the integrated code.

The internal coupling method provides a high level of accuracy and parallelism. The disadvantage of this method is that enormous code modification is required, and there is limited access to source codes. External coupling is accomplished through a user interface module where data is transferred between two codes without modification. The advantage of the external method is that both codes can maintain their independence during the procedure (Ye *et al.*, 2020). Due to its simplicity, the external coupling method is applied in the study.

## 4.2 North Anna

### 4.2.1 Geometry

The North Anna PWR reactor is well documented, similar to Koeberg PWR, and is selected as the reference (Mulasi, 2022). The core contains 157 Fuel Assemblies (FA) and each fuel assembly is arranged in a 17x17 lattice. Each fuel assembly consists of 264 fuel rods with an active fuel length of 364.998 cm, and these fuel rods are supported by grids at intervals along their length to maintain spacing between the rods in the assembly. The fuel rods are cladded by Zircaloy-4, and their properties are listed in Table 2-1.

There are 24 guide thimbles and one instrument thimble positioned in the centre. The guide tubes and thimble plugs are channels that allow for the insertion of control rods, burnable poison rods, or neutron sources (VEPCO, 2016). Table 4-1 lists the geometry of the fuel pin and assembly used in the model.

**Table 4-1: Fuel pin and assembly geometry** (VEPCO, 2016)

| | Value | Units |
|---|---|---|
| Fuel pellet outer diameter | 0.40958 | cm |
| Cladding inner diameter | 0.41783 | cm |
| Cladding outer diameter | 0.47498 | cm |
| Fuel rod pitch | 1.25984 | cm |
| Active fuel height | 364.998 | cm |
| Fuel rods per assembly | 264 | - |
| Guide thimbles per assembly | 24 | - |
| Instrument thimbles per assembly | 1 | - |
| Assembly pitch | 21.471 | cm |
| Assemblies per core | 157 | - |

### 4.2.2 Material composition

#### 4.2.2.1 Fuel $UO_2$

North Anna has three fuel enrichments, namely 2.1, 2.6, and 3.1 wt. %, the highest enrichment of 3.1 wt. % is used for this model to be more conservative. The fuel composition is calculated in atom density using Equation 3-3. The fuel material composition for the solid reference model is

listed in Table 7-1 of Appendix A. Each model in the study will have a different fuel composition due to different fuel enrichment.

The theoretical density for $UO_2$ with natural uranium is 10.96 g/cm$^3$. From the North Anna data, it was found that the theoretical density of the fuel is 95% (VEPCO, 2016); therefore, the natural uranium oxide density is multiplied by 0.95 to get the actual density of the fuel, which is used to calculate the atom density for the fuel composition (NEA, 2022).

### 4.2.3 H/HM

The H/HM ratio for the solid reference fuel pin and assembly was computed using dimensions from Table 4-1. The water area around the fuel pin was calculated using Equation 3-5 to determine the H/HM ratio. Equation 3-4 was used to calculate the ratio, where the fuel pin H/HM ratio is 5.78, and the assembly is 6.69.

### 4.2.4 Neutronic model

The North Anna PWR is modelled in sections. One fuel pin from 264 fuel pins is isolated from the fuel assembly to model it in 3D. The reactor core has 157 fuel assemblies; only one is modelled in 3D. Fuel pin and assembly dimensions listed in Table 4-1 are used for the modelling. Material compositions used are either calculated or retrieved from the Serpent built-in material library.

#### 4.2.4.1 Boundary conditions

##### 4.2.4.1.1 Fuel pin

The study's three fuel pin models use the same neutron source points and boundary conditions.

- Boundary conditions are reflective in the x and y direction and black (vacuum) in the z-direction.
- Neutron source points for the fuel cell in the simulation are 25000 with 800 active and 450 inactive cycles. The simulation uses these numbers to achieve source convergence by looking at the plot of Shannon entropy vs cycles. See Section 4.6.3.

##### 4.2.4.1.2 Fuel assembly

The study's three different fuel assembly models all use the same neutron source points and boundary conditions.

- Boundary conditions for the fuel assemblies' array with 17x17 and 13x13 fuel pins are reflective in the x and y direction and black in the z-direction.

- The fuel assembly does not contain reflectors on the top and bottom.
- Neutron source points for the fuel assembly in the simulation are 100000, with 2500 active and 400 inactive cycles. The simulation uses these numbers to achieve source convergence by looking at the plot of Shannon entropy vs cycles. See Section 4.6.3.

#### 4.2.4.2 Power

The power output of the full core North Anna reactor is 2893 MWth. The reactor has 157 fuel assemblies; thus, the power is divided by the number of assemblies to get the power per assembly. 264 fuel rods make up a fuel assembly. To calculate the average power per fuel pin, the power of the fuel assembly is divided by the number of rods. Table 4-2 lists the power calculated for the solid reference model (VEPCO, 2016).

**Table 4-2: North Anna power**

| | Value | Units |
|---|---|---|
| North Anna core power | 2893000 | kW |
| Power per assembly | 18426.75 | kW |
| Power per rod | 69.79 | kW |

#### 4.2.4.3 Temperature

The temperatures of all the materials used in the solid reference model are listed in Table 4-3. The temperatures were assumed constant in radial and axial directions but will be discretised for the coupling calculations later, as discussed in Section 4.5. All the burnup models in this study will use the same constant temperatures.

**Table 4-3: Average temperatures of different materials (Bowman and Suto, 1996)**

| Material | Temperature (K) |
|---|---|
| Fuel | 901 |
| Cladding | 629 |
| Water | 583 |

### 4.2.5 Burnup model

The burnup model is created using the 3D model input for the fuel pin and the fuel assembly. The model requires volumes for all materials in the input, and the fuel material is divided into eight radial sub-zones of equal volume. All the models in the study have the same radial sub-zone division for the fuel material; however, the volumes vary depending on the model. The solid reference fuel pin and assembly burnup models use the powers listed in Table 4-2. Two approaches were followed, the total fissile content is kept the same and the enrichment is kept the same.

The study aims to compare fuel models' safety and operational characteristics. The economic evaluation hinges on the assumption that the power level at which burnup was modelled and the total fissile content in the core was kept at the same level for all the pin and fuel assembly models. This facilitates economic evaluation based on burn-up or full power days. The total fissile content was corrected (with less fuel in the annular fuel models) by increasing the enrichment levels accordingly. This approach would entail different power densities in the fuel pins since the enrichment and mass of fuel in the models are different, as well as the number of pins per assembly. It must be noted that the aim is to generate the same power level and maintain the same core and fuel assembly dimensions for the proposed annular fuels.

It would be possible to keep the fuel enrichment constant across the fuel models, but that would lead to shorter fuel cycles since annular fuel has a smaller volume and mass than the reference fuel. The second approach was followed and compared between the reference and helium annulus models, as seen in Section 5.1.1.

### 4.2.6 Thermal-hydraulic model

#### 4.2.6.1 Materials

##### 4.2.6.1.1 $UO_2$ thermal conductivity

The Flownex input requires thermal conductivity for the fuel ($UO_2$). Equation 4-1 is used to compute the thermal conductivity at different temperatures.

$$\lambda\left[\frac{W}{m.K}\right] = \frac{100}{7.5409 + 17.692\tau + 3.6142\tau^2} + \frac{6400}{\tau^{5/2}} \exp\left(\frac{-16.35}{\tau}\right) \quad 4\text{-}1$$

a) (Kavazauri *et al.*, 2016)

b) (Nuclear power, 2022e)

4.2.6.1.2 $UO_2$ specific heat capacity

Equation 4-2 is recommended for the correlation of $UO_2$ heat capacity. Table 4-4 provides the values of the constants used in that equation.

$$C_P(T)\left[\frac{J}{Kg.K}\right] = C_1 * \left(\frac{\theta}{T}\right)^2 * \frac{\exp\left(\frac{\theta}{T}\right)}{\left[\exp\left(\frac{\theta}{T}\right)-1\right]^2} + 2C_2T + C_3E_a\exp\left(-\frac{E_a}{T}\right)/T^2 \quad \text{4-2}$$

where $T$ is the temperature (K), $\theta$ is Einstein temperature (K) and $E_a$ is the electron activation energy divided by the Boltzman constant (K).

**Table 4-4: Constant used in heat capacity (Popov *et al.*, 2000)**

| Constant | $UO_2$ | Units |
|---|---|---|
| $C_1$ | 302.27 | J/Kg/K |
| $C_2$ | $8.463\times10^{-3}$ | $J/Kg/K^2$ |
| $C_3$ | $8.741\times10^{7}$ | J/Kg |
| $\theta$ | 548.68 | K |
| $E_a$ | 18531.7 | K |

4.2.6.1.3 Helium specific heat capacity

Zircaloy-4 cladding is sealed with helium gas in the gaps under pressure equal to or more than 2.5 MPa (Gabr *et al.*, 2003). Flownex has built-in helium heat capacity at various pressure and temperatures. However, helium properties at 2.5 MPa are required. Heat capacity at 2 MPa and 3 MPa is available. The average of 2 MPa and 3 MPa is 2.5 MPa; thus, the average specific heat capacity at these two pressures gives us that at 2.5 MPa.

4.2.6.1.4 Helium thermal conductivity

Thermal conductivity is computed at 2.5 MPa. Flownex has thermal conductivity built-in at 2 and 3 MPa. The average thermal conductivity of helium at 2 MPa and 3 MPa gives that at 2.5 MPa.

#### 4.2.6.1.5 Zircaloy-4

Flownex has a Zirconium built-in material library. Zircaloy-4 is one of the Zirconium alloys, and the properties are assumed to be the same.

#### 4.2.6.1.6 Water

The Flownex code master database lists water ($H_2O$) in the charts and tables. However, the flow rate through the assembly must be determined. The solid reference model's total core flow rate is provided in the safety report (VEPCO, 2016). The total core flow rate is divided by the number of fuel assemblies to determine the flow rate per fuel assembly. Further, the fuel assembly is divided by the number of fuel pins in a fuel assembly to get the flow rate in each fuel pin. It was assumed that the flow through the guide tubes channels is the same as the flow through fuel pins channels. For more accurate flow rate through the guide tube calculations shall be considered in the future.

## 4.3 Water annulus fuel pin

MIT proposed using a fuel pin with a gap in the middle to pass coolant through, to reduce central heat accumulation, as discussed in Chapter 2 Section 2.3.1. The details of the water annulus model will be described.

### 4.3.1 Material composition

#### 4.3.1.1 Fuel $UO_2$

Fuel enrichment for this model is determined by calculation and compared to the North Anna fuel enrichment. The total number of fuel pins and the fuel area in the assembly are compared to the North Anna reference and provide the fuel assembly volume ratio. The enrichment is scaled according to the volume to keep the total fissile content and power as close to North Anna as possible. North Anna fuel enrichment divided by the fuel assembly volume ratio gives the water annulus model fuel enrichment of 3.4 wt. %. The fuel composition is calculated in atom density using Equation 3-3 and listed in Table 7-2 of Appendix A.

#### 4.3.1.2 SiC

SiC is used in this model as fuel cladding. Serpent has built-in material compositions for some materials used in the nuclear industry. However, SiC is one of those materials that are not listed. For this model, the composition of SiC was calculated using Equation 3-3. Table 7-5 in Appendix

A lists the composition of SiC as used in the Serpent model. SiC cladding composition was used on all annular fuel models.

### 4.3.2 H/HM

Equations 3-4 and 3-5 are used on various fuel assembly arrays to calculate H/HM for the water annulus fuel pin and fuel assembly, as shown in Table 2-3 and Table 2-4. The water annulus fuel assembly's H/HM ratio is 8.24, whereas that for the fuel pin is 7.67. The 13x13 array fuel pin and assembly dimensions are closer to the reference and the H/HM ratio. Therefore, the 13x13 array was chosen for the water annulus fuel model.

### 4.3.3 Neutronic model

The water annulus pin model is modelled in sections as well. The reactor core has 13x13 fuel assemblies with 160 fuel pins each.

#### 4.3.3.1 Power density

The design aims to use the same reactor core fundamental dimensions and parameters as the reference. The solid reference's pin power is used to calculate the power density for the water annulus fuel pin (VEPCO, 2016). The fuel volume is determined using the fuel pin's dimensions. The theoretical density for annular fuels is 94 %; therefore, 0.94 of the natural uranium density and the volume are used to determine the mass and the actual fuel density. (Feng *et al.*, 2017). Power and mass give power density for the fuel pin and assembly. as shown in Table 4-5. The power density values are used in the water and helium annulus models.

**Table 4-5: Power density calculation**

| | Value | Units |
|---|---|---|
| North Anna core power | 2893000 | kW |
| Power per assembly | 18426.75 | kW |
| No. of fuel assemblies | 157 | - |
| Fuel density | 10.41 | $g/cm^3$ |
| Volume per assembly | 50782.16 | $cm^3$ |
| Mass per assembly | 528743.84 | g |
| Power per pin | 69.79 | kW |
| Rods per assembly | 264 | - |
| Volume per pin | 192.36 | $cm^3$ |
| Mass per pin | 2002.82 | g |
| Rod power density | 0.04385 | kW/g |
| Assembly power density | 0.04385 | kW/g |

## 4.4 Helium annulus fuel pin

The helium annulus fuel pin model depicted in Figure 4-1 right, was adapted from the water annular fuel model with internal and external cooling discussed in Section 2.3.1 and Section 4.3. There are numerous expected design and manufacturing issues with the water annulus pin, such as the sealing of the fuel rod and production cost. The water annulus fuel pin has two surfaces that need cladding as depicted in Figure 4-1 left, has implications for manufacturing, cost, neutron absorption, and flow distribution. The concern in PWRs today is leaking fuel pins. Since the cladding surface of water annulus fuel pins is increased by a significant margin and the end welds are more complicated, this could potentially also increase the fuel pin leak statistics. It was decided to alter the dimensions of the water annulus fuel pin with internal and external cooled fuel and achieve a H/HM ratio as close as possible to the reference North Anna reactor.

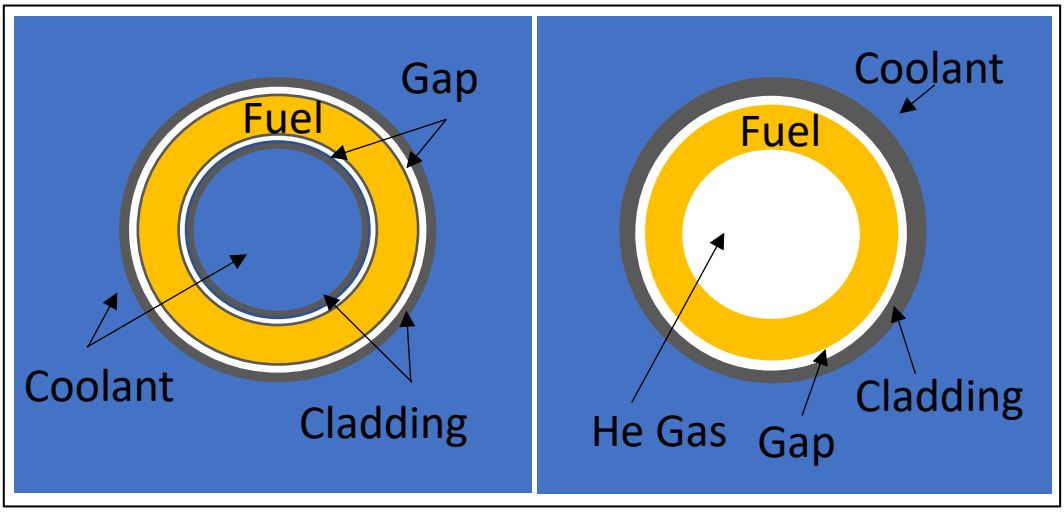


**Figure 4-1: Water annulus fuel (left) and helium annulus fuel pin (right)**

### 4.4.1 Material composition

#### 4.4.1.1 Fuel $UO_2$

The same procedure used in Section 4.3.1.1 to calculate the fuel enrichment for the water annulus model was also applied to the helium annulus model. This resulted in a fuel enrichment for the helium annulus fuel pin of 4.0 wt.%. The fuel composition was calculated in atom density using Equation 3-3 and listed in Table 7-3 of Appendix A.

Preliminary calculations showed that a better burnup could be achieved with the helium pin, and it was decided to also test the helium annulus with the same enrichment as the reference. Similarly, the fuel composition was calculated in atom density and listed in Table 7-4 of Appendix A.

### 4.4.2 H/HM

Table 4-6 and Table 4-7 contain the adapted helium annulus fuel pin, assembly dimensions from references in Table 2-2 and the H/HM ratio for various arrays. Guide thimbles dimensions adapted for this model are the same as those for the solid reference and the water annulus models. The units used for the dimensions are cm. A designate area, and R is the radius. The subscripts ci, f, and co designate inner cladding, fuel, and outer cladding; the second subscript designates the outer (o) or inner (i) surface.

**Table 4-6: Helium annulus pin dimensions and H/HM ratio**

| Array | Dfi | Dfo | Dci | Dco | Pitch | H/HM pin |
|---|---|---|---|---|---|---|
| **11x11** | 1.2000 | 1.7000 | 1.7124 | 1.8267 | 1.9520 | 3.122898 |
| **12x12** | 1.0800 | 1.5400 | 1.5524 | 1.6667 | 1.7890 | 3.222869 |
| **13x13** | 1.0000 | 1.3600 | 1.3848 | 1.4991 | 1.6460 | **4.348914** |
| **14x14** | 0.8800 | 1.2940 | 1.3064 | 1.4207 | 1.5330 | 3.251142 |
| **15x15** | 0.8000 | 1.1978 | 1.2102 | 1.3245 | 1.4310 | 3.230963 |

**Table 4-7: Helium annulus fuel assembly dimensions and H/HM ratio**

| Array | No. guide tubes | No. fuel pins | R in guide | R out guide | Pitch | H/HM Assembly |
|---|---|---|---|---|---|---|
| **11x11** | 7 | 114 | 0.5715 | 0.61214 | 21.4720 | 3.66353 |
| **12x12** | 8 | 136 | 0.5715 | 0.61214 | 21.4680 | 3.56436 |
| **13x13** | 9 | 160 | 0.5715 | 0.61214 | 21.3980 | **4.97613** |
| **14x14** | 12 | 184 | 0.5715 | 0.61214 | 21.4620 | 3.80507 |
| **15x15** | 20 | 205 | 0.5715 | 0.61214 | 21.4650 | 4.01654 |

For the helium annulus models, the 13x13 array is employed. The H/HM ratios of the helium annulus fuel pin and assembly are lower than those of the solid reference fuel pin and water annulus fuel pin due to the removal of the water and cladding in the inner annulus. As seen in Table 4-6 and Table 4-7 the ratio of the fuel pin is 4.35 at the 13x13 fuel assembly array, and the assembly is 5.01, which are the highest numbers among the examined arrays.

### 4.4.3 Thermal-hydraulic model

#### 4.4.3.1 SiC thermal conductivity

Two methods for calculating the SiC thermal conductivity were attempted. Firstly, the thermal conductivity of SiC cladding is calculated at 2.5 MPa using Equation 4-3 (Li, 2013). This method is for the SiC with high pure and dense poly-crystals, where the thermal conductivity in Figure 2-3 of Chapter 2 is the highest curve.

$$\boldsymbol{k(T) = [-0.0003 + 1.05 * 10^{-5}T]^{-1}} \qquad 4\text{-}3$$

Where $K(T)$ is the thermal conductivity of SiC (W/mK) and $T$ is the cladding temperature (K).

Secondly, data was extracted from Figure 2-3, representing the lowest curve with poly-crystal grains. Data from both methods are used in separate Flownex SiC thermal conductivity inputs to investigate the effect of thermal conductivity on the coupled temperatures.

#### 4.4.3.2 Water

Flownex uses $H_2O$ from the master database. The method stated in Section 4.2.6.1.6 is used to calculate the flow rate, although there are 160 fuel pins and 9 guide tubes in this case. Furthermore, the flow rate is adjusted closer to the reference models. The flow rate and other parameters must be the same as the reference because the design seeks to keep the core the same. It is assumed that the flow through the guide tube channels is the same as for the fuel pin channels for this study.

## 4.5 Coupling methodology

This section discusses the coupling methodology for the solid reference and helium annulus fuel pins. The water annulus fuel pin model was not considered for coupling due to findings in neutronic calculations; from the beginning to the end of life, the model produced $k_{eff}$, and reactivity higher than the reference. The H/HM ratio for this model is also higher. The solid reference and helium annulus fuel pin models are discussed in Sections 4.2 and 4.4, and they are verified in Section 4.6.4 to calculate steady-state conditions in Flownex.

The illustrated coupling procedure follows and is shown in Figure 4-1.

1. MobaXterm was used to create and run Serpent calculations through the High-Performance Computer (HPC).
2. Serpent input for the solid reference fuel pin was created using the 3D input model, as shown in Table 7-7 Appendix D.
3. Temperatures and densities in the first iteration are assumed constant at first. The Cool.ifc input file was created and linked to the solid reference fuel pin file. The coolant densities and temperatures of the fuel pin at 10 axial nodes are specified in this file. The cool.ifc file is shown in Table 7-8 of Appendix D. The same axial nodes are applied in the helium annulus fuel pin input.
4. The input file Fuel.ifc was created and linked to the solid reference fuel pin file. The temperature of the 7 radial rings in the fuel pin are specified in this file. The fuel.ifc input file is shown in Table 7-9 Appendix D. In the helium annulus fuel pin, 8 radial rings are applied.

5. The Serpent inputs are run, and the code produced output files. From the cool.ifc output file, power distribution at each axial node is read and verified that the Serpent powers equate to calculated total power.
6. The Flownex model was set up, and all parameters and material compositions were specified.
7. The power distribution from the cool.ifcout Serpent file was used in the Flownex input file to specify power distribution.
8. Run steady-state conditions and Flownex produced two output files. The first file contains coolant densities and temperatures as in Table 7-10 Appendix E. The second file is for the fuel and cladding temperatures in 10 axial nodes and 7 radial (70 temperature points in the fuel material, 10 for the gap and 10 for the fuel cladding) as demonstrated Figure 7-5 Appendix E. In the helium annulus fuel pin case, Flownex produced 80 temperature points in the fuel material, 10 for the gap and 10 for the fuel cladding.
9. The densities and temperatures from Flownex are input into Serpent cool.ifc and fuel.fic files to calculate the power at the right temperatures, and the iteration process continues until convergence is reached, where the error needs to be less than 2%.
10. As discussed in Section 2.6, adaptive relaxation was used for the models to reach convergence.
11. The same process was followed for the helium annulus fuel pin coupling.

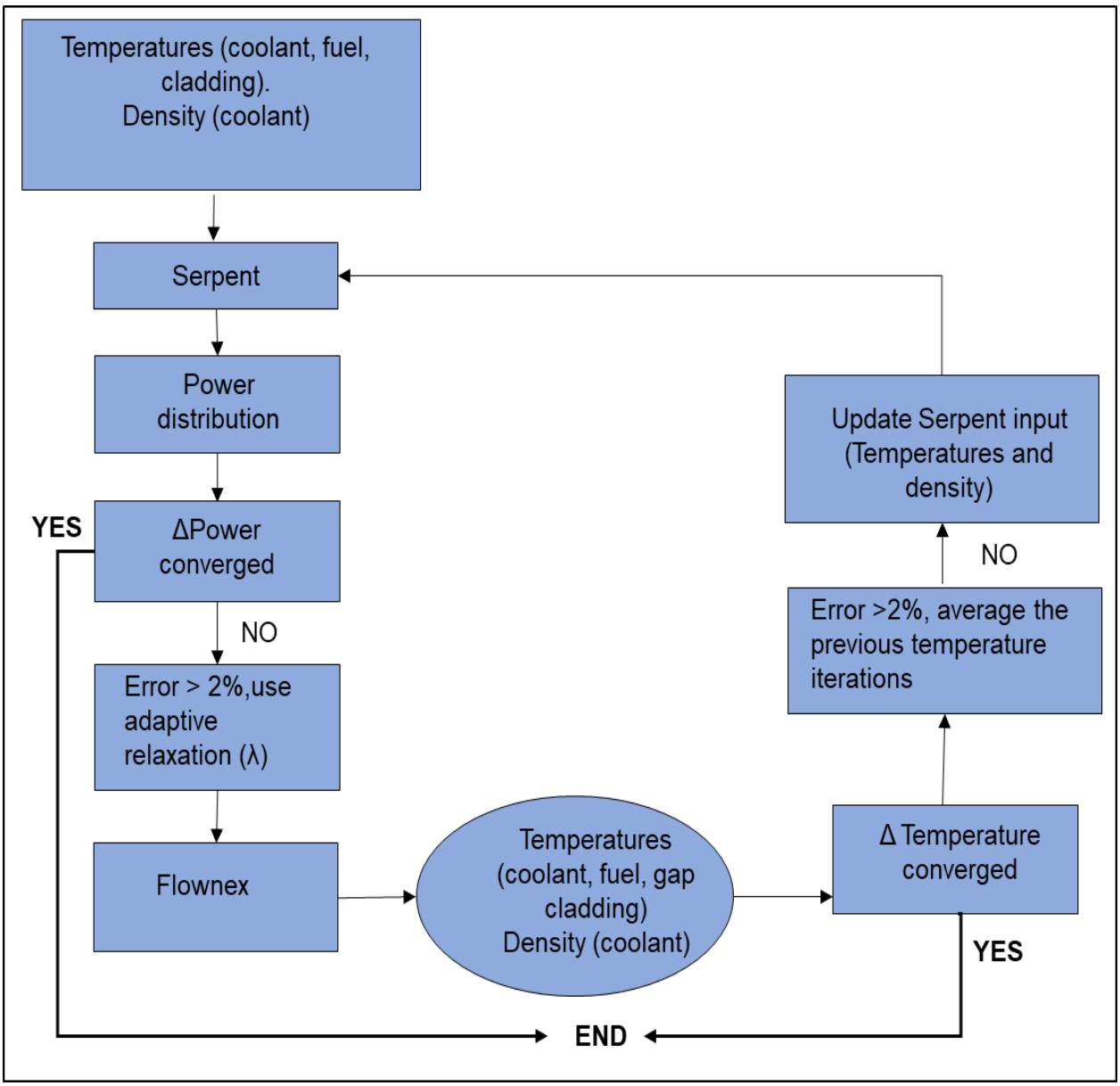


**Figure 4-2: Coupling methodology between Serpent and Flownex**

## 4.6 Verification

### 4.6.1 Geometry plots

Position parameters and minimum and maximum coordinates in the input define the boundaries of the plot region and produce geometry plots in png format. Each material on the geometry is plotted with a different colour. The colours are defined using the rgb entry in the material card. The geometry is used to verify that the input numbers are correct, producing an image representing the fuel pin and assembly.

#### 4.6.1.1 Fuel pins

Serpent produces top and side view images for the fuel pin and assembly. The yellow circle represents the fuel pellet and the helium gaps are white, and the coolant is shown in blue, while the fuel cladding is shown in grey in Figure 4-3, Figure 4-4, and Figure 4-5. Figure 4-3 displays the solid reference fuel pin, and the water annulus fuel pin is depicted in Figure 4-4. The adopted helium annulus fuel pin is shown in Figure 4-5.

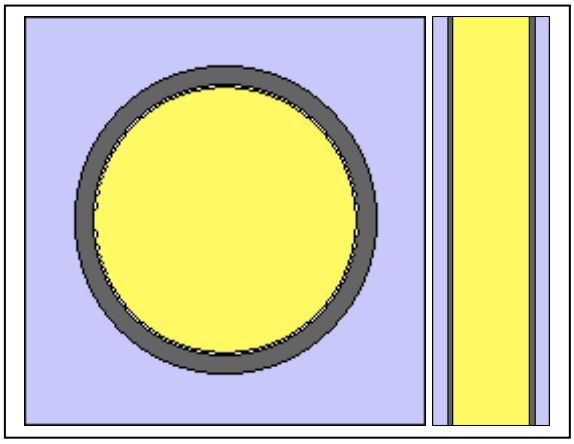

**Figure 4-3: Solid reference fuel pin top and side view**

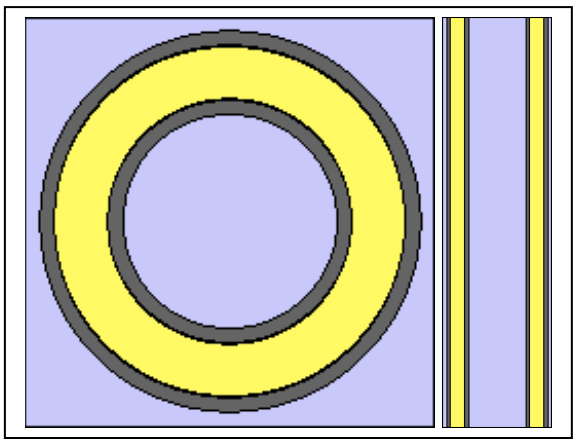

**Figure 4-4: Water annulus pin top and side view**

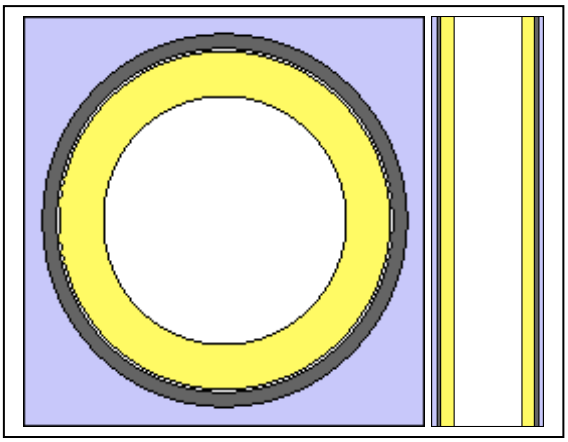

**Figure 4-5: Helium annulus pin top and side view**

The geometry plots showing the top and side views of the fuel pins produced by Serpent are faultless, and 3D input files are verified.

#### 4.6.1.2 Fuel assemblies

The North Anna reactor core fuel assemblies are arranged in a 17x17 assembly lattice. The annular fuel design uses a lattice of 13x13. The solid reference fuel assembly's fuel pins can be recognized as the yellow circle, and the guide and instrumentation thimbles/guide as the blue circle in Figure 4-6.

Figure 4-7 depicts the top and side views of the water annulus fuel assembly. The annular fuel models have nine guide thimbles/tubes, while the solid has 24. The guide thimbles/tubes can be identified in red circles in Figure 4-7 and Figure 4-8 for the water and helium annulus fuel assemblies.

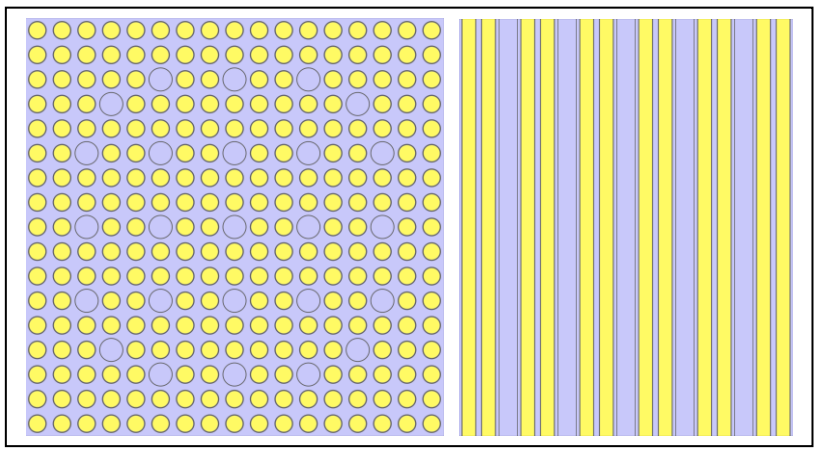

**Figure 4-6: Solid reference fuel assembly top and side view**

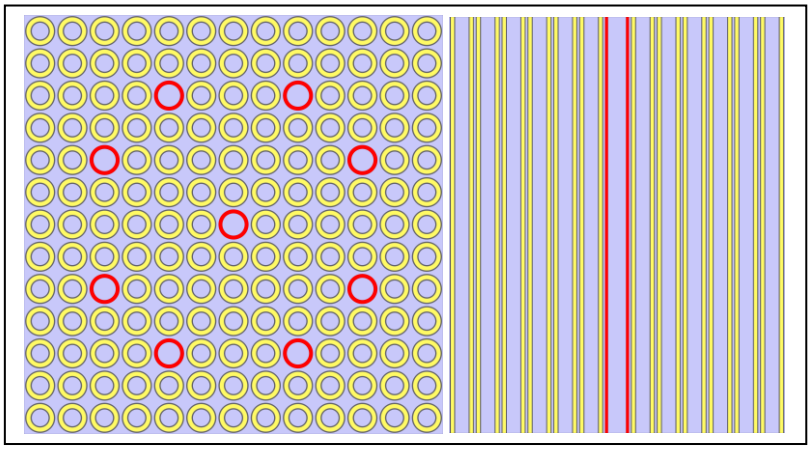

**Figure 4-7: Water annulus fuel assembly top and side view**

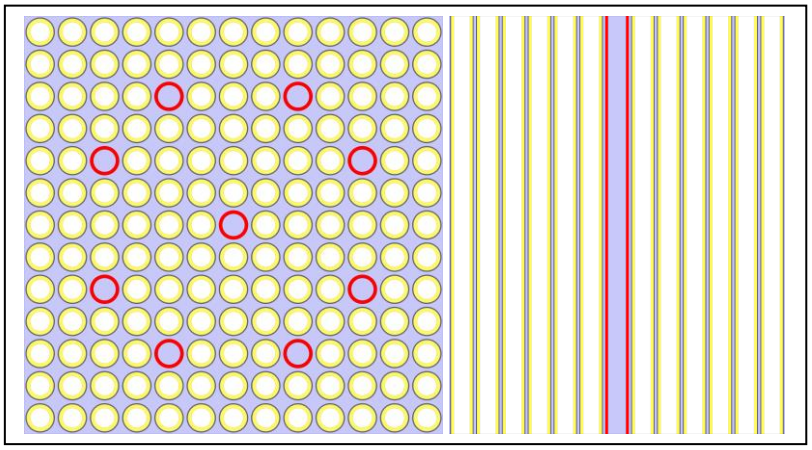

**Figure 4-8: Helium annulus fuel assembly top and side view**

The solid reference fuel assembly is a 17x17 array with 24 guide tubes and one instrument tube in the middle. Figure 4-6 verifies the model geometry for the fuel assembly. Annular fuel assemblies are 13x13 with 8 guide tubes and one instrument tube. Figure 4-7 and Figure 4-8 verify the two annular fuel assembly geometries respectively.

#### 4.6.1.3 Burnup div cards

The burnable fuel material for all three fuel pins and assembly models was divided into eight radial depletion sub-zones, as illustrated in Figure 4-9. In a burnup calculation, all occurrences are treated as a single depletion zone if the material is not divided. Fuel material division for burnup models' geometry is verified.

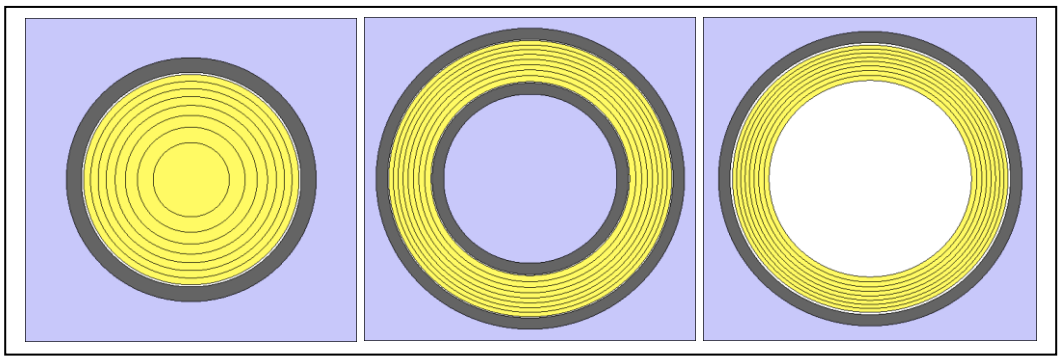

**Figure 4-9: Fuel division of the solid, water, and helium annulus pins**

### 4.6.2 Volumes

Verification of material volumes is required before the burnup model can be compiled. Serpent produces volumes from the 3D model. To verify the volumes produced by Serpent, one needs to calculate volumes using Equation 4-4 of a cylinder for the solid fuel pin and Equation 4-5 for the annular fuels. Table 4-8, Table 4-9, and Table 4-10 list calculated and Serpent material volumes and the errors for all the models in the study.

$$V = \pi r^2 h \qquad 4\text{-}4$$

$$V = \pi(R1^2 - R2^2) \qquad 4\text{-}5$$

**Table 4-8: Solid reference fuel pin and assembly material volumes**

| Material | Calculated volume ($cm^3$) | Serpent volume ($cm^3$) | Error (%) |
|---|---|---|---|
| **Fuel pin** | | | |
| **Fuel** | 192.36 | 192.53 | 0.09 |
| **Helium gap** | 7.83 | 7.86 | 0.36 |
| **Zircaloy-4** | 58.51 | 58.65 | 0.24 |
| **Water** | 323.54 | 320.29 | 1.02 |
| **Fuel assembly** | | | |
| **Fuel** | 50782.16 | 50788.10 | 0.01 |
| **Helium gap** | 2067.66 | 2054.63 | 0.68 |
| **Zircaloy-4** | 16908.83 | 16775.10 | 0.57 |
| **Water** | 98590.57 | 97689.50 | 0.92 |

**Table 4-9: Water annulus fuel pin and assembly material volumes**

| Material | Calculated volume ($cm^3$) | Serpent volume ($cm^3$) | Error (%) |
|---|---|---|---|
| **Fuel pin** | | | |
| **Water** | 213.70 | 214.42 | 0.34 |
| **SiC inner** | 60.27 | 60.29 | 0.03 |
| **Helium gap** | 6.99 | 7.16 | 2.28 |
| **Fuel** | 288.96 | 288.95 | 0.00 |
| **Helium gap** | 10.07 | 9.94 | 1.29 |
| **SiC outer** | 97.05 | 96.61 | 0.45 |
| **Water** | 317.87 | 317.54 | 0.10 |
| **Fuel assembly** | | | |
| **Water** | 34191.99 | 34190.80 | 0.00 |
| **SiC inner** | 9643.18 | 9694.12 | 0.53 |
| **Helium gap** | 1119.07 | 1110.40 | 0.78 |
| **Fuel** | 46233.94 | 46039.30 | 0.42 |
| **Helium gap** | 1610.93 | 1611.45 | 0.03 |
| **SiC outer** | 16400.89 | 15572.00 | 0.29 |
| **Water** | 59262.95 | 59922.10 | 1.10 |

**Table 4-10: Helium annulus fuel pin and assembly material volumes**

| Material | Calculated volume ($cm^3$) | Serpent volume ($cm^3$) | Error (%) |
|---|---|---|---|
| **Fuel pin** | | | |
| **Helium** | 286.67 | 286.60 | 0.01 |
| **Fuel** | 243.55 | 243.02 | 0.00 |
| **Helium gap** | 19.51 | 19.71 | 0.05 |
| **SiC** | 94.58 | 94.44 | 0.14 |
| **Water** | 344.58 | 345.11 | 0.03 |
| **Fuel assembly** | | | |
| **Helium** | 45867.00 | 45757.20 | 0.24 |
| **Fuel** | 38968.60 | 38988.00 | 0.05 |
| **Helium gap** | 3122.21 | 3157.29 | 1.11 |
| **SiC** | 15132.88 | 15116.50 | 0.11 |
| **Water** | 63536.11 | 64138.60 | 0.94 |

The solid reference model calculated volumes agree well with the Serpent volumes. The error between the calculated and Serpent volume for the fuel in an assembly is 0.01 %. The water annulus model calculated volumes agree with the Serpent volumes. However, the error in the helium gap is slightly higher. The adapted helium annulus fuel model calculated volume agree

with the Serpent volumes and the errors between all materials range is 0.00 – 1.11%. The calculated volumes and the Serpent are close, and all the models are verified.

### 4.6.3 Shannon entropy

Shannon entropy plots are used to verify that the source has converged. Shannon entropy vs cycle plots for the three fuel pin and assembly models are presented in Appendix C. Figure 7-3 A-C represent the convergence of the three fuel pins, where A is the solid reference fuel pin, B is the water annulus fuel pin, and C is the helium annulus fuel pin. The Shannon entropy plots for fuel assemblies are presented in Appendix C Figure 7-4 D-F, where D is the solid fuel assembly, E is the water annulus fuel assembly, and F is the helium annulus fuel assembly.

### 4.6.4 Coupling methodology

The fuel pin models are divided into axial nodes and radial rings. The aim is to determine the power distribution, coolant density, and temperature at each point in the pin. Figure 4-10 on the left shows the fuel is divided into 7 radial rings and the one on the right shows that the fuel pin is divided into 10 axial nodes for the solid reference fuel pin. The helium annulus fuel pin material is divided into 8 radial rings and 10 axial nodes, as shown in Figure 4-11.

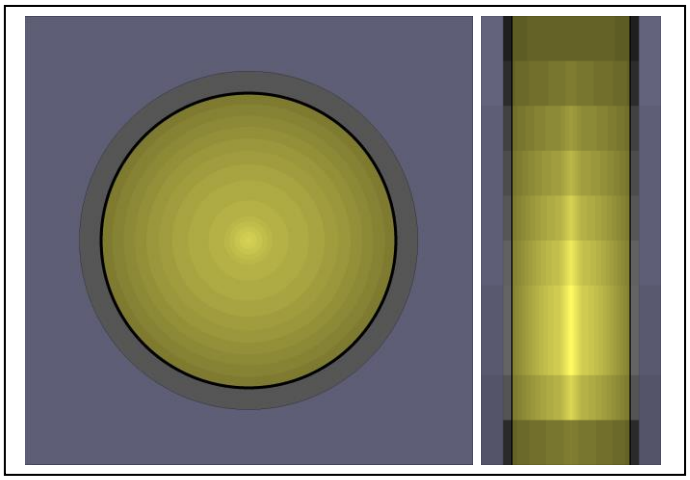

**Figure 4-10: Solid fuel pin radial and axial view**

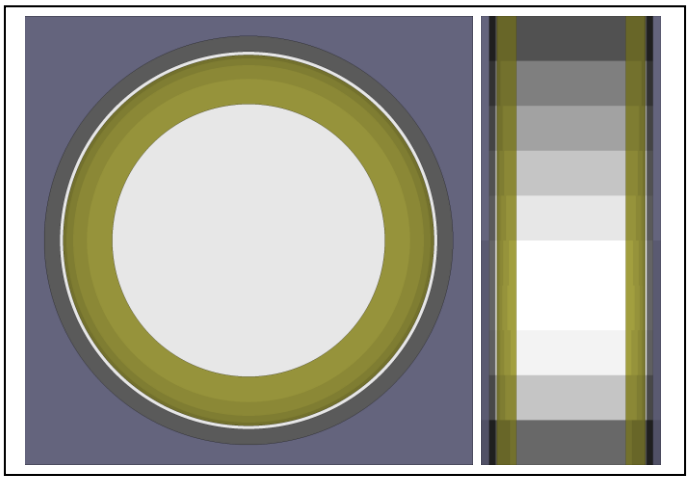

**Figure 4-11: Helium annulus pin radial and axial view**

The radial and axial division of the fuel material was successful, as depicted in Figure 4-10 and Figure 4-11, and the model geometry is verified.

## 4.7 Conclusion

The neutronic and thermal-hydraulic models for the fuel pins and assemblies were discussed in detail, codes used and the coupling methodology. Verification of volumes, geometry plots, convergence through Shannon entropy and material div cards were also discussed.

# CHAPTER 5

# RESULTS AND DISCUSSION

### Overview

This chapter discusses results such as burnup and fuel temperature distributions. The solid reference fuel pin results are compared to the literature and the two annular fuels on a pin level and fuel assembly level.

## 5.1 Neutronic parameters

### 5.1.1 3.1 wt % fuel enrichment

A burnup model with 3.1 wt. % fuel enrichment was developed for the fuel pin and assembly models to evaluate burnup and cycle length of the helium annulus fuel against the reference. The results of these models are presented in Appendix B. The burnup results are shown in Table 7-6, indicating that at the Beginning of Life (BOL), the helium annulus fuel models both have $\boldsymbol{k_{eff}}$ slightly less than the reference models. At the End of Life (EOL), the fuel pin and assembly models for the helium annulus models achieved a higher burnup of 75 MWd/kgU. However, the cycle length of these models is 231 and 214 Effective Full Power Days (EFPD) shorter than the reference models.

The higher burnup indicates a better fuel utilisation, and the reduced cycle length is due to less initial fissile content and the reduced total mass of heavy metal in annular fuel models.

The shorter fuel life cycle is a disadvantage. A higher fuel enrichment was considered as an alternative. A fuel enrichment of 4.0 wt. %, for the helium annulus, corresponds to the total fissile mass of the reference. This enrichment was used for the coupling of helium annulus fuel models.

### 5.1.2 4.0 wt % fuel enrichment

#### 5.1.2.1 Fuel pin

Burnup models were developed to evaluate the variation of $\boldsymbol{k_{eff}}$ with burnup for the fuel pins and assemblies. The solid reference model's enrichment is 3.1 wt. %, the water annulus model's fuel enrichment is 3.4 wt. % and the helium annulus model's enrichment is 4.0 wt. % based on equivalent fissile content. Burnup results for the fuel pins are shown in Table 5-1.

**Table 5-1: Fuel pins burnup results**

| | BOL ($k_{eff}$) | EOL ($k_{eff}$) | Burnup (MWd/kgU) | Time (EFPD) |
|---|---|---|---|---|
| **Reference solid** | 1.3071 | 0.8140 | 66.3 | 1676.9 |
| **Water annulus** | 1.3089 | 0.8133 | 71.3 | 1624.8 |
| **Difference** | **0.0019** | **-0.0006** | **5** | **-52.1** |
| | | | | |
| **Helium annulus** | 1.3127 | 0.8140 | 80.0 | 1541.9 |
| **Difference** | **0.0057** | **-0.0000** | **13.8** | **-134.9** |

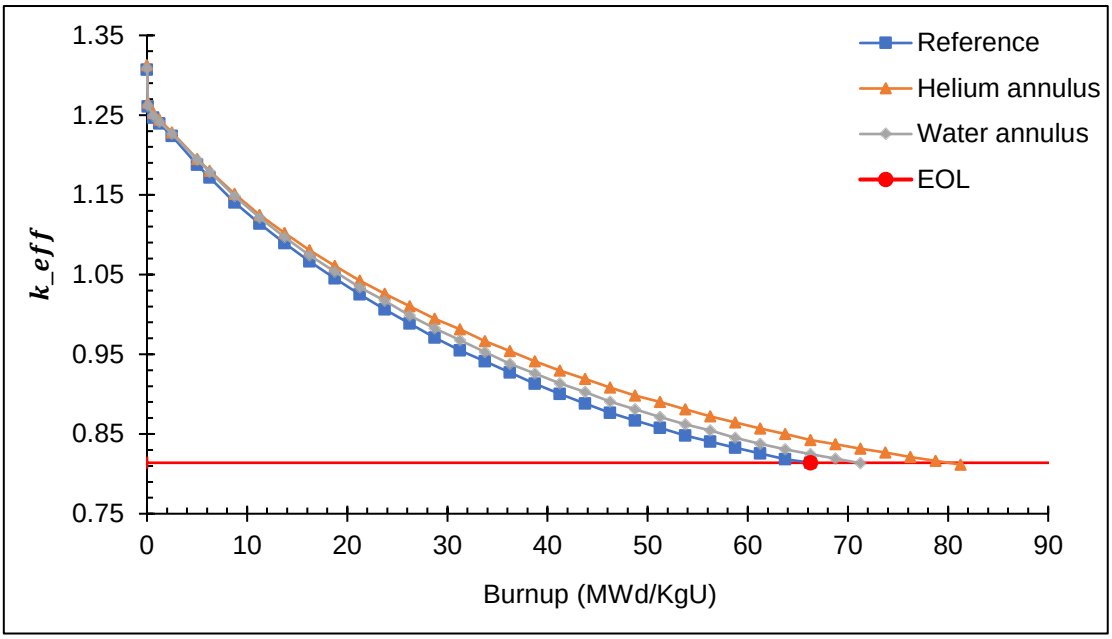


**Figure 5-1: Variation of $k_{eff}$ with burnup for the fuel pins**

For this study, fresh fuel was used, and re-loading was not considered. The EOL line designates the EOL of the reference fuel in Figure 5-1. At BOL, the solid reference and water annulus fuel pins have a slightly lower $k_{eff}$ compared to the helium annulus pin. The water annulus fuel pin achieved a burnup of 71 MWd/kgU, 5 MWd/kgU higher than the solid reference fuel pin with a burnup of 66 MWd/kgU, as shown in Table 5-1. The water annulus pin model's fuel cycle length is 1625 EFPD, 51.2 EPFD shorter than the solid reference pin model.

The helium annulus fuel pin achieved a slightly higher $k_{eff}$ at the BOL compared to the solid reference and water annulus due to the observed better fuel utilisation. The helium annulus fuel pin could achieve a higher burnup of 80 MWd/kgU compared to the solid reference and water annulus pins. However, the fuel life cycle length of the helium annulus at the EOL is 1542 EFPD,

135 EFPD shorter than the solid reference. The helium annulus fuel achieves a significantly higher burnup than the reference and water annulus fuel. It seems likely that the shorter fuel cycle can be compensated by increasing the fuel enrichment or using alternative fuel such as Thorium – such investigation is beyond the scope of this work.

El-Sahlamy *et al.*, studied solid and water annulus fuel pins with a 17x17 assembly array for the solid and 13x13 for the water annulus fuel pin. The $k_{eff}$ for the solid and water annulus fuel pin at the BOL is 1.39390 and 1.3759 respectively (El-Sahlamy *et al.*, 2020). The calculated solid reference fuel pin and water annulus fuel pin do not agree with that of the literature. In the study by El-Sahlamy et al., a fuel enrichment of 4.95%, Monte Carlo N-Particle Transport code 6 (MCNP6) and Reactor Excursion and Leak Analysis Program (RELAP5) codes were used. Temperatures of 900 K was used for the solid fuel and 600 K for the annular fuel. The water temperature of 583.1 K for both fuel pin models were assumed. Boron was used with a concentration of 1000 ppm (El-Sahlamy *et al.*, 2020). Fuel enrichment of 3.1 wt% and 4.0 wt% were used in the study on separate models, which is less than the one used in literature.

**Table 5-2: Fuel assembly burnup results**

| | BOL ($k_{eff}$) | EOL ($k_{eff}$) | Burnup (MWd/kgU) | Time (EFPD) |
|---|---|---|---|---|
| **Reference** | 1.3317 | 0.7978 | 66.3 | 1675.6 |
| **Water annulus** | 1.3236 | 0.7987 | 73.8 | 1673.5 |
| **Difference** | -0.0081 | 0.0009 | 7.5 | -2.1 |
| | | | | |
| **Helium annulus** | 1.3419 | 0.7977 | 85.0 | 1633.3 |
| **Difference** | 0.0103 | -0.0001 | 18.8 | -42.3 |

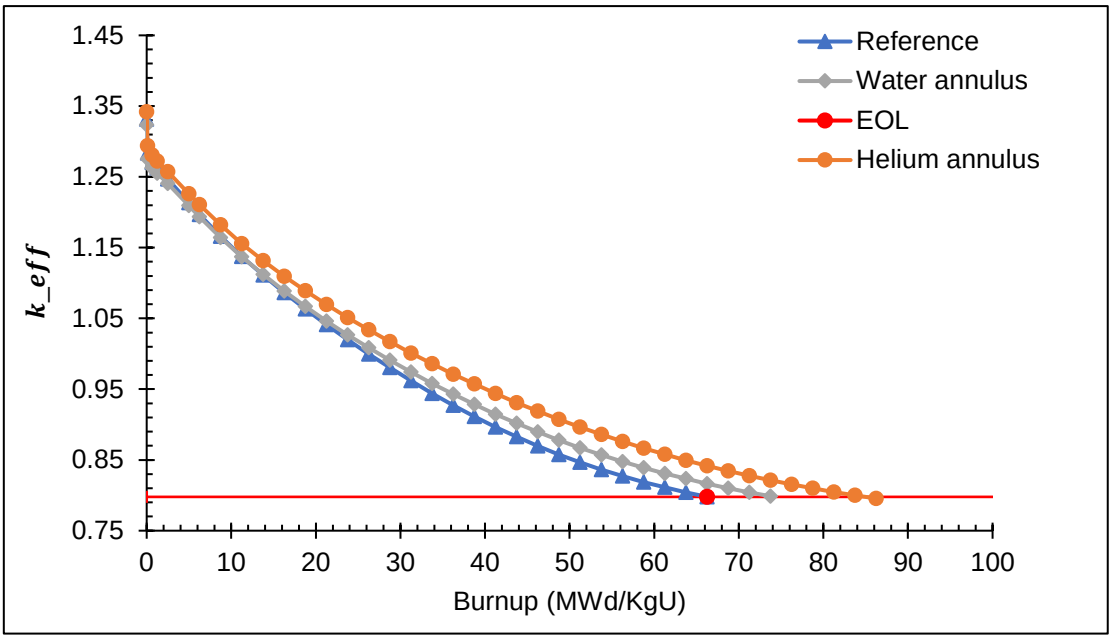


**Figure 5-2: Variation of $k_{eff}$ with burnup for fuel assemblies**

The fuel assembly models do not contain reflectors at the top and bottom. Similar to pin models, fresh fuel was used, and re-fuelling was not considered. The variation of $k_{eff}$ with burnup for the fuel assemblies almost follows a similar pattern compared to fuel pin models, as seen in Figure 5-2. At BOL, the helium annulus fuel assembly achieves a slightly higher $k_{eff}$ than the water annulus and solid reference fuel assemblies. The helium annulus achieves a higher burnup of 85 MWd/kgU with a life cycle of 1633 EFPD, 42.3 EFPD shorter than the reference fuel, as shown in Table 5-2.

As found for the 3.1 wt% enriched fuel in all models, the higher burnup indicates a better fuel utilisation, and the reduced cycle length is due to less initial fissile content and the reduced total mass of heavy metal in annular fuel models. The increase in enrichment and hence the increase in initial fissile content, somewhat improved cycle length of the annular models compared to the 3.1 wt% models.

The short life fuel cycle of the helium annulus fuel assembly can be compensated by using fuel assemblies with different fuel enrichment in the reactor core. Increasing fuel volume can also be considered to improve the cycle length.

## 5.2 Coupling

### 5.2.1 Power distribution

#### 5.2.1.1 Solid reference pin

In this study, the fuel pin power distribution was calculated as a function of the axial node and used in the thermal-hydraulic code to obtain the temperature and density of the coolant and fuel and cladding temperature in each node. The coupling process for the solid reference fuel pin's power distribution was computed from iterations 1 to 6, where λ=0.5 was used in Serpent calculations. The power peak distribution is at the bottom part of the fuel pin. In some iterations, the peak is towards the centre of the fuel pin, and the error between iterations 1 to 9 is much larger. The power converges at iteration 10 with a maximum error of 2.08% and an average error of 1.08%, as shown in Figure 5-3. Initially, it was aimed to reduce the maximum error between iterations 1 and 6 to below 2%. However, the error remained large, and an effort was made to further reduce this error by reducing the parameter λ to 0.3 in iterations 7 to 10. These iterations rendered a maximum error of 2.08% in iteration 10, and it was decided to use the obtained values. Refinement of the obtained errors is recommended for future study. It must be noted that while adaptive relaxation is introduced to assist with power convergence equally, the temperatures from the previous iterations are averaged to assist with temperature convergence.

Liu and Cai utilised a one-dimensional axial single channel model to simulate the Supercritical Water Reactor (SCWR) double-row assembly, which featured the fuel pin, coolant, and moderator channels. After 19 iterations, the linear power density in this study converged at λ =0.35. λ=0.4 was adapted for the first 16 iterations where the factor was not steady to guarantee convergence (Liu and Cai, 2013).

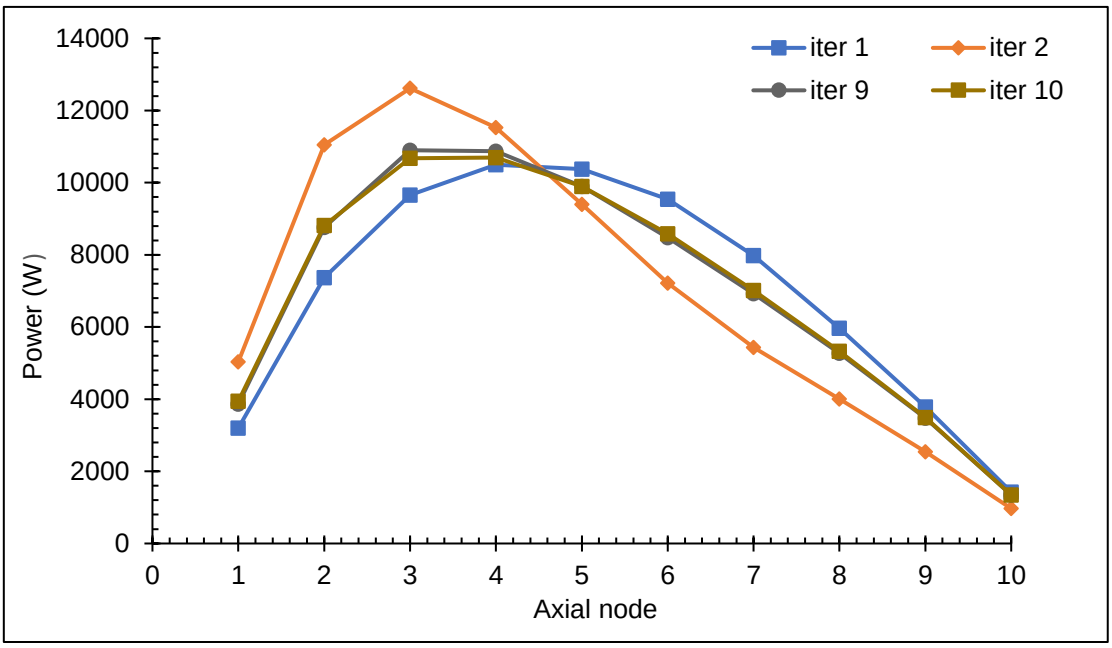


**Figure 5-3: Axial power distribution for the solid reference fuel pin**

#### 5.2.1.2 Helium annulus pin

The helium annulus fuel pin was divided into 10 axial nodes, just as the solid reference fuel pin. The coupled calculation for this model converged to below 2% after 10 iterations. This model is adapted from the water annulus fuel pin model and does not have a particular study in literature to compare with; however, it is compared to the solid reference model in this study. Coupling for this model started with λ=0.5 from iterations 1 to 6, where the power distribution oscillates between iterations 1 to 4, as shown in Figure 5-4. The power distribution starts to converge between iterations 5 and 6; however, the error is still significantly large. λ=0.3 is introduced in iterations 7 to 10, and the power distribution converges with a maximum error of 0.91% and an average error of 0.50%. The helium annulus models' power distribution converged with errors of less than 2% and less than the solid reference.

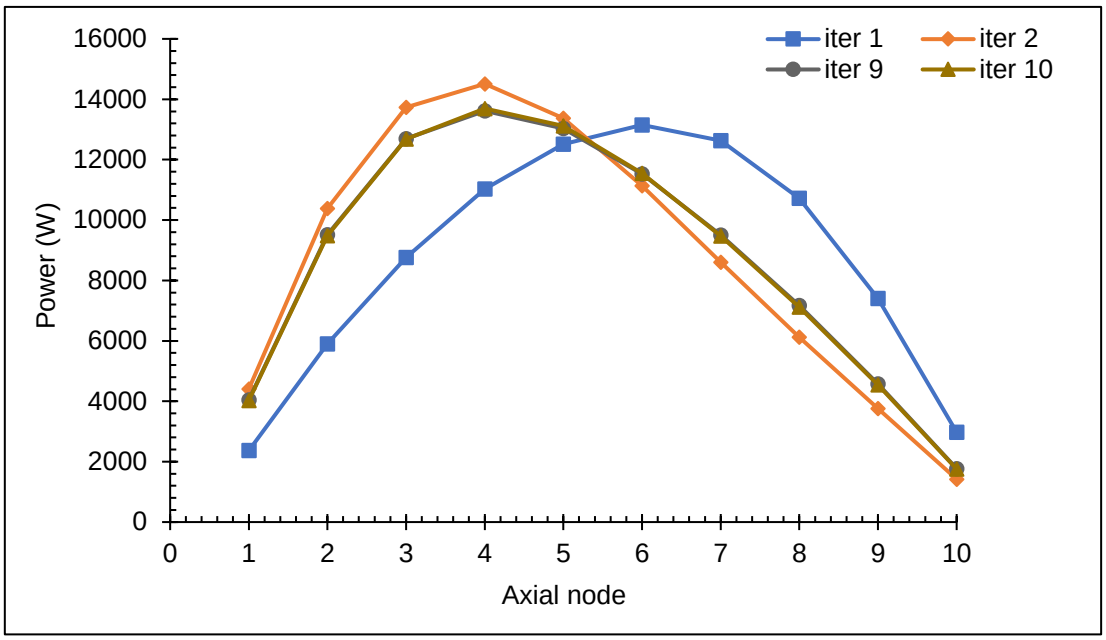


**Figure 5-4: Axial power distribution for helium annulus fuel pin**[4]

### 5.2.2 Convergence

#### 5.2.2.1 Solid reference pin

The solid reference fuel pin was coupled for 10 iterations, and two values for λ were used between iterations. λ=0.5 was used in the first 6 iterations; however, errors in iterations 1 to 2 are high due to temperatures not being averaged. In iterations 3 to 9, average temperatures are used, and a decrease in the maximum errors is observed. From Figure 5-5, conclusions can be made that λ=0.5 errors are larger (iterations 1 to 6) than λ=0.3 (iterations 7 to 10); thus, using small λ is recommended when using the adaptive relaxation method. The maximum converged error for the solid reference fuel pin is slightly larger than the expected error in the study, but the average error in the iterations is as expected.

[4] Iterations 9 and 10 are coincident lines (lie on top of each other)

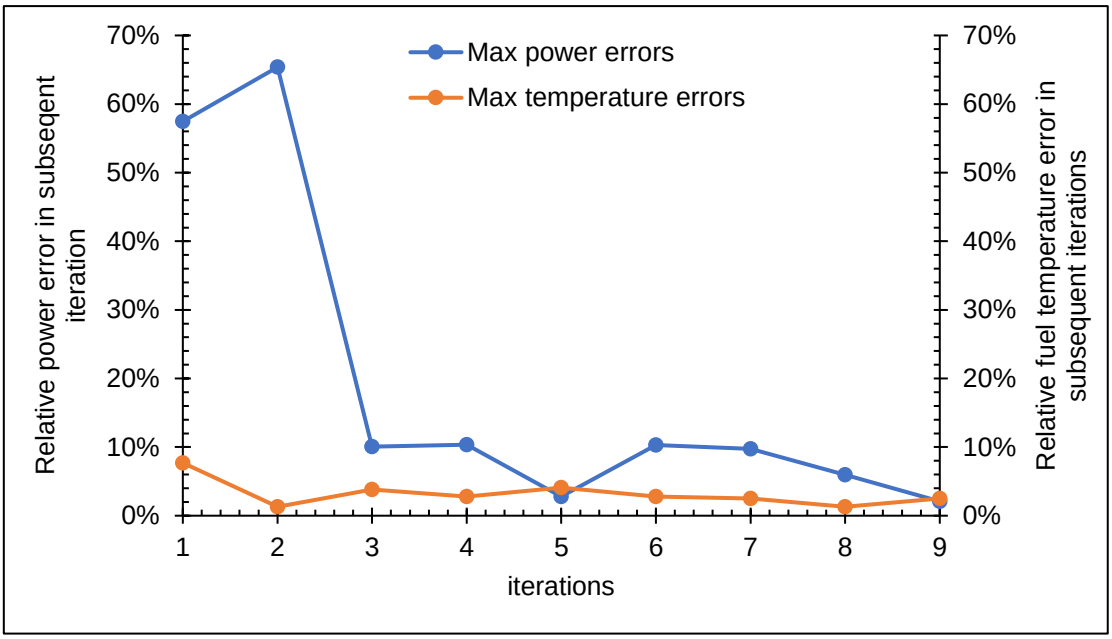


**Figure 5-5: Relative power and fuel temperature error in subsequent iterations of the solid reference fuel pin**

#### 5.2.2.2 Helium annulus pin

A similar pattern is observed in Figure 5-6, where the first two iterations of the helium annulus fuel pin errors are high for the same reason as the solid reference pin. However, the errors for this fuel pin are below the study's expected maximum error of 2%. Two values for λ were used between iterations: for iterations 1 to 7, a value of λ=0.5 was applied, and for iterations 8 to 10, a value of λ=0.3 was used. Similarly, a conclusion can be made that iterations with λ=0.5 (iterations 1 to 6) have larger errors than iterations with λ=0.3 (iterations 7 to 10); thus, using a small λ is recommended when using the adaptive relaxation method.

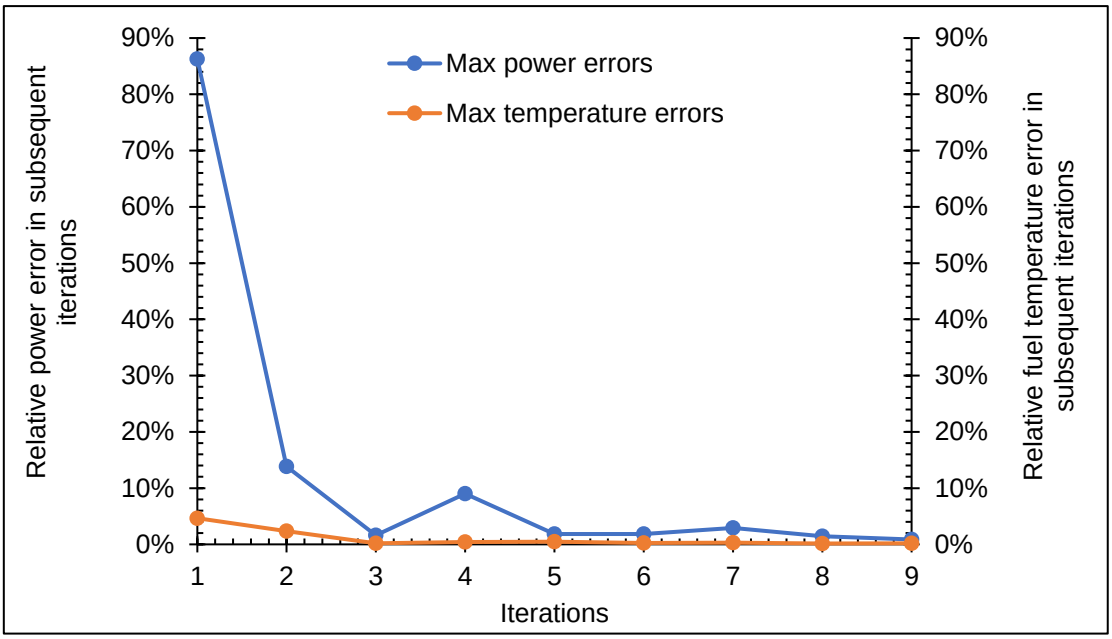


**Figure 5-6: Relative power and fuel temperature in subsequent iterations of the helium annulus fuel pin**

### 5.2.3 Coolant temperatures

Coolant temperature influences neutron moderation: when the coolant density decreases due to an increase in coolant temperature, neutron moderation decreases, which causes a decrease in power deposition. The coolant flows from the bottom to the top in the reactor core; thus, the axial temperature distribution increases with height, as seen in Figure 5-7. The maximum coolant temperature is 602.2 K for the solid reference fuel pin. Liu and Cai studied the convergence of neutron/thermal-hydraulic coupling on SCWR and found that the coolant temperature with axial height converged at a temperature of 783 K for the solid fuel pin and recommended that the same coupling methodology applies to PWRs calculations (Liu and Cai, 2013).

The maximum coolant temperature for the helium annulus model is 602.2 K. The helium annulus fuel pin achieved the same maximum coolant temperature as the solid reference fuel pin, as depicted in Figure 5-7, confirming that the power level is correct.

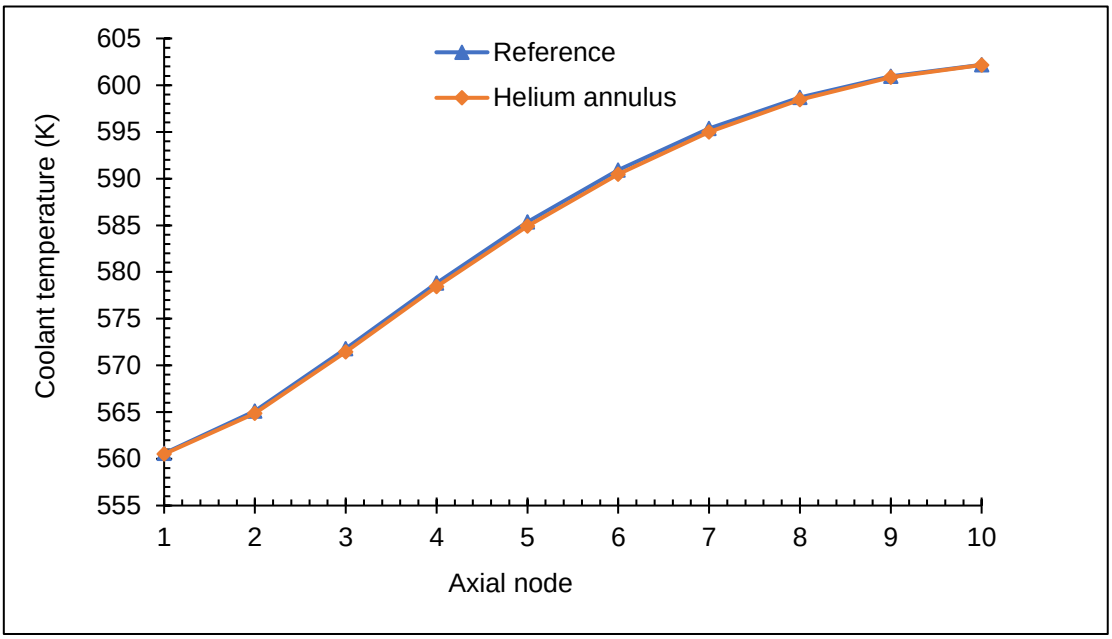


**Figure 5-7: Coolant temperature distribution of the fuel pins**

### 5.2.4 Axial fuel temperature

The maximum fuel centreline temperature for the solid reference fuel pin from the converged iteration is 2372.7 K. This maximum temperature is below the fuel melting temperature of 3073.2 El-Sahlamy *et al.*, coupled neutronic and thermal-hydraulic models (MCNP6 and RELAP5) using a 17x17 solid fuel assembly PWR similar to the reference in this study and found the fuel centreline temperature to be 2476.2 K (El-Sahlamy *et al.*, 2020). The solid reference fuel pin maximum fuel temperature is 103.5 K less and is in good agreement with the literature. This validates that the coupling methodology is correct.

The helium annulus fuel pin does not have a centreline because of the annulus in the centre. The maximum fuel temperature is read at the point $T_{f_i}$ as illustrated in Figure 2-7. From the converged iterations, the maximum fuel temperature of the helium annulus fuel pin is 1216.3 K. Yarmohammadi *et al.*, used a fuel pin similar to the helium annulus pin to study the effect that the hole in the centre has on fuel temperature distribution and found the maximum fuel temperature as 1848 K (Yarmohammadi *et al.*, 2017). The results agree fairly well with the literature depending on the dimensions and power level. Figure 5-8 illustrate the fuel centreline temperature of the solid reference and the maximum fuel temperature of the helium annulus fuel pins.

The helium annulus fuel pin's maximum fuel temperature is further compared to the solid reference fuel pin, which is 1156.4 K. The lower peak maximum temperature for the helium annulus depicted in Figure 5-8 is an advantage of the annular fuels. More grace time during

abnormal operation or accident conditions is achieved with lower peak temperatures. This lower fuel temperature renders better fuel performance and lower fission gas release.

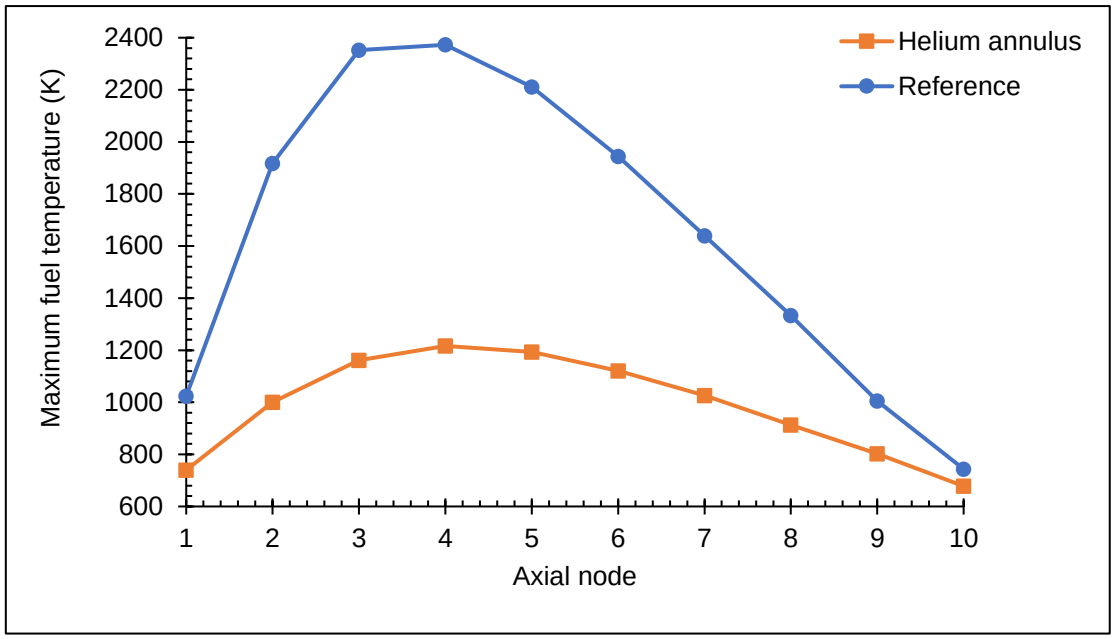


**Figure 5-8: Axial fuel temperature**

### 5.2.5 Radial fuel temperature

Radial fuel temperature distribution in the hot channel for the solid reference and helium annulus fuel pins is shown in Figure 5-9. The maximum temperatures are the same as the those in axial.

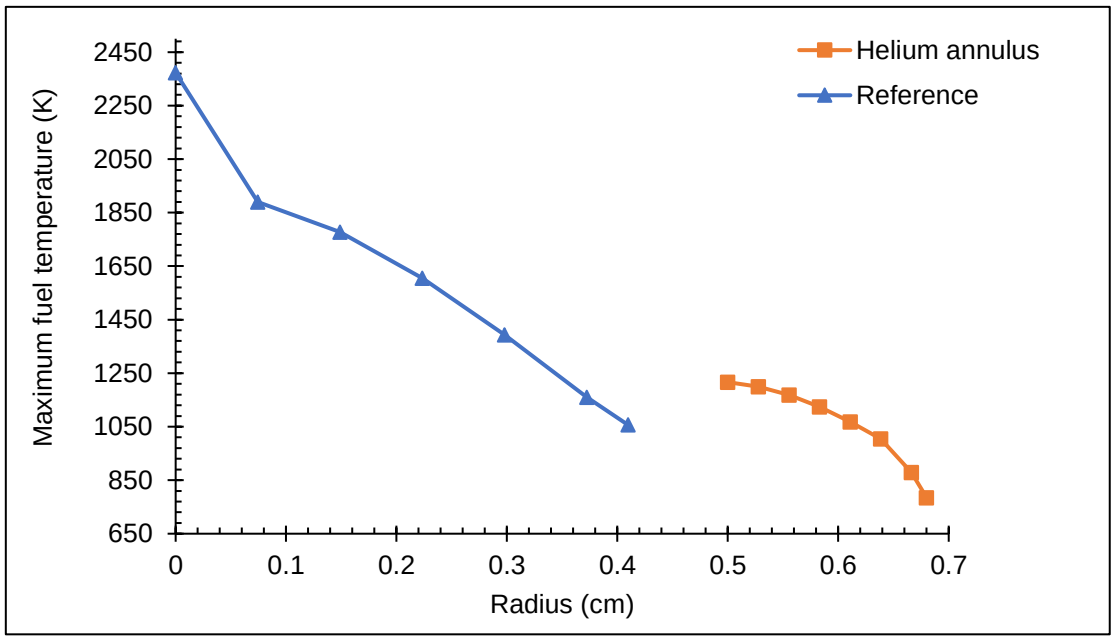


**Figure 5-9: Radial fuel temperature distribution**

### 5.2.6 Surface cladding temperature

The solid reference fuel pin used Zircaloy-4 cladding. The surface cladding temperature is proportional to the fuel temperature. Surface cladding temperature increases when the fuel temperature increases, as shown in Figure 7-6 Appendix F, and the maximum surface cladding temperature is 702 K. A similar published study using the same solid fuel pin rendered a surface cladding temperature of 632 K (El-Sahlamy *et al.*, 2020).

The helium annulus model uses SiC fuel cladding. This SiC cladding thermal conductivity has two forms, small and large grains. Two separate helium annulus models were coupled, SiC thermal conductivity with small grains and SiC with large grains, as discussed in Sections 2.2.2.1 and 4.4.3.1. The two maximum surface cladding temperatures are compared to evaluate if the thermal conductivity grain size influences the cladding temperature. The surface cladding temperature of SiC thermal conductivity with small grains and the one with large grains are similar, the difference in these temperatures is negligible given uncertainties. The maximum surface cladding temperature is 603 K. The helium annulus fuel pin surface temperature is 99 K lower compared to the solid reference surface cladding. The helium annulus fuel pin's surface cladding and coolant temperatures are similar, as shown in Figure 7-7 Appendix F. The SiC cladding has lower temperatures and does not produce hydrogen gas in the case of transient or accident conditions.

## 5.3 Conclusion

Three fuel pin and assembly models with different fuel enrichment results were analysed and compared. Based on neutronic results, the helium annulus fuel assembly achieved higher burnup of 85 MWd/kgU than the solid reference and water annulus fuel assemblies, with the same amount of fissile content. It was therefore decided to continue investigating the helium annulus in terms of thermal hydraulics. The coupling process of the two fuel pin models was successful with the adaptive relaxation method. In thermal-hydraulics, maximum /centreline fuel temperature is one of the important parameters. ATF aims to reduce central heat accumulation and fuel melting. The helium annulus fuel pin has reduced central heat due to a maximum fuel temperature of 1216 K, significantly lower than the solid reference with maximum temperature of 2373 K. In addition to the improved safety characteristics, a better fuel utilisation is achieved by virtue of a significant improvement in burnup. The slight reduction in EFPD is deemed insignificant and can be improved by slightly increasing enrichment.

# CHAPTER 6

# CONCLUSION AND RECOMMENDATIONS

### Overview

This chapter recaps the aim of the study, draws conclusions on the results and makes further recommendations for future study.

## 6.1 Conclusion

In the following steps, the study aimed to evaluate SiC cladded annular fuels as ATF for PWRs using neutronic and thermal-hydraulic analyses.

A 3D neutronic model for the solid fuel pin and assembly with Zircaloy-4 cladding was developed using North Anna fuel pin dimensions. Burnup models for the same fuel pin and assembly were also developed, with fuel enrichment at 3.1 wt. %. Coupling was introduced between Serpent and Flownex for the models' neutronic and thermal hydraulic analysis. The coupling methodology achieved the goal set out by the study. The solid reference models were assessed, and the results agreed with the published findings.

Next, 3D fuel pin and assembly models for annular fuel with internal and external cooling were developed using known published fuel pin dimensions. The fuel pin dimensions of the water annulus fuel pins used in this study are slightly bigger than the reference; thus, the fuel assembly array is 13x13. Burnup models were also developed for the fuel pin and assembly. Based on the neutronic analysis and physical design aspects, the water annulus fuel pin was not considered for coupling. The Water annulus fuel pin with Zircaloy-4 cladding brings a much higher Zirconium charge to the reactor core, increasing hydrogen formation in accident scenarios; therefore, an alternative fuel cladding is required. It is expensive to produce annular fuel, even more so when SiC cladding is used to replace Zircaloy-4, as it is difficult to seal SiC materials during fuel fabrication.

Due to the challenges related to water annulus models, the helium annulus model was further developed. The model only has external cooling, and the gap in the centre is filled with helium gas. The fuel pin dimensions were adapted from the water annulus model and adjusted to achieve H/HM ratios as close to the reference as possible. 3D fuel pin, assembly, and burnup models were developed for the helium annulus. This model used 4.0 wt.% fuel enrichment, SiC fuel

cladding and 13x13 fuel assembly array. The H/HM ratio for this model rendered H/HM values less than the reference.

The coupling of Serpent and Flownex was introduced, and the same coupling methodology used for the reference was applied to the helium annulus. Two separate coupling input files for this model were created due to differences in the thermal conductivity grain size of SiC cladding. The aim was to test if the grain size of the SiC cladding thermal conductivity would affect the surface cladding. Temperature profiles of the helium annulus fuel pin with large grain SiC cladding thermal conductivity are similar to the profiles of the helium annulus fuel pin with small grains SiC cladding thermal conductivity. The difference in these temperatures is negligible, given uncertainties.

The helium annulus model results were compared to the reference; in the coupling exercise, this model converged below an error of 2% in both power and fuel temperature distributions. The helium annulus fuel pin has the advantage of maximum fuel temperatures 1216 K lower than the solid reference fuel pin with of 2373 K.

All the models in the study were verified in terms of geometry plots, volumes, fuel pin dimensions, and Shannon entropy. The combination of Serpent and Flownex provided similar results to published results from other studies.

The helium annulus fuel pin with SiC cladding has proven to be a suitable replacement for the solid reference fuel pin with Zircaloy cladding. The model produced maximum temperatures lower than the reference, and the same applied to surface cladding and coolant temperatures. The fuel pin achieved higher burnup with the same fuel enrichment as the reference with less fuel cycle length. The fuel pin’s H/HM ratio is lower than that of the solid reference, and by using SiC fuel cladding, no hydrogen gas will be produced in accident conditions.

## 6.2 Recommendations

**Solid reference fuel pin**

The neutronic study included pin and fuel assembly models, i.e., boronated water, reflectors, and burnable absorber were not modelled. It is recommended that the model be extended to the full core. The solid reference fuel pin converged with a maximum error above the study's expected error. More iterations are recommended while decreasing the λ used in the adaptive relaxation method to reach convergence below 2 % error between consecutive coupling iterations.

The North Anna model was tested using Zircaloy-4, which is an outdated fuel cladding. The current PWRs use more recent Zirconium alloys. It is recommended that the model be tested using these zirconium alloys.

It was assumed that the flow in the guide tubes is the same as for the fuel pins, when calculating the flow rate of the coolant. For more accurate flow rate, it is recommended that these calculations take into consideration the flow through the guide tubes.

**Water annulus fuel pin**

The water annulus fuel pin models achieve similar burnup to the reference; however, they cannot be qualified due to unknown fuel and cladding temperatures. Therefore, coupling for this model is recommended.

More research on the techno-economic feasibility of fuel fabrication of the water annulus fuel pin is required.

**Helium annulus fuel pin**

The neutronic study on this model was limited to pin and assembly models without using boronated water, reflectors, and burnable absorber. It is recommended that modelling be expanded to full core models for criticality and burnup studies. The model was coupled using a neutronic (Serpent) code and a thermal-hydraulic (Flownex) code. Further investigations can be done, which would provide a level of verification if, e.g., alternative high-fidelity neutronic codes such as MCNP and thermal-hydraulic codes like RELAP 3D be used. It is recommended that a fuel performance study be done on this model. Since the helium annulus model was only analysed under normal conditions, it is recommended that analyses be done for transient conditions as well. Adequate safety coefficients for reactivity feedback and reactivity control need to be investigated.

At the EOL, the helium annulus fuel models achieved burnup in a shorter fuel cycle length than the solid reference. Therefore, the appropriate addition of thorium to the fuel is recommended to be investigated as a possible solution to increase burnup and cycle length.

The study can also be extended to perform the depletion calculations with the coupled code system, so that the advantages of a lower average fuel temperature on the cycle length can also be confirmed. This may negate the shorter cycle length. Finally it is recommended that the study includes multi-cycle 3D coupled calculations.

# BIBLIOGRAPHY


Abdalla, A. (2012) ‘Sensitivity Analysis of Fuel Centerline Temperatures in SuperCritical Water-cooled Reactors (SCWRs)’.

Allison, B. (2013) ‘Operator generic fundamentals’. Available at: https://slideplayer.com/slide/4681548/.

Ansarifar, G. R. *et al.* (2016) ‘Investigation of the dual-cooled annular fuel effect on the thermal power uprate in a VVER-1000 nuclear reactor’, *Nuclear Technology*, 195(1), pp. 105–109. doi: 10.13182/NT15-90.

ATI Metals (2015) ‘Zircaloy-4 Annealed - Technical Data Sheet’, 1, pp. 2014–2016. Available at: https://www.atimetals.com/Products/Documents/datasheets/zirconium/alloy/Zr_nuke_waste_disposal_v2.pdf.

Beydoğan, N. *et al.* (2016) ‘Pin Cell Simulation of the Change in Doppler Broadening and Self-Shielding with the Change in Nuclear Fuel Temperature and Fuel Type by Using OpenMC’, 21(1), pp. 25–28.

Bowman, S. . and Suto, T. (1996) ‘SCALE-4 Analysis of Pressurized Water Reactor Critical Configurations ’:, 5.

Brown, F. B. (2006) ‘On the Use of Shannon Entropy of the Fission Distribution for Assessing Convergence of Monte Carlo Criticality Calculations’.

Carmack, J. (2016) ‘Update on U. S. Accident Tolerant Fuel Program’, *Nuclear Regulatory Commission Briefing Office of Nuclear Energy*. Available at: http://www.hydrogen.energy.gov/nuclear.html.

Carpenter, D. M. (2006) *Assessment of Innovative Fuel Designs for High Performance Light Water Reactors*.

Deng, Y. *et al.* (2020) ‘THERMAL-HYDRAULIC MODEL OF ANNULAR FUEL OF PRESSURIZED HEAVY WATER REACTOR’, *Nuclear Engineering and Technology*, (xxxx). doi: 10.1016/j.net.2020.06.025.

Deng, Y. *et al.* (2021) ‘Design and evaluation of an innovative LWR fuel combined dual-cooled annular geometry and SiC cladding materials’, *Nuclear Engineering and Technology*, 53(1), pp. 178–187. doi: 10.1016/j.net.2020.06.025.

Dobisesky, J. *et al.* (2014) ‘Fuel management of pwr cores with silicon carbide cladding’, *Nuclear Technology*, 186(3), pp. 353–377. doi: 10.13182/NT12-131.

El-Sahlamy, N. *et al.* (2020) ‘Comparison between standard solid fuel and a new annular fuel performance in the core of a PWR’, *Kerntechnik*, 85, pp. 161–168. doi: 10.3139/124.190020.

Ellis, T. S. (2006) *Advanced Design Concepts for PWR and BWR High-Performance Annular Fuel Assemblies*. Massachusetts Institute of Technology. Available at: https://dspace.mit.edu/handle/1721.1/41268 (Accessed: 14 May 2021).

Feng, D. *et al.* (2017) ‘Thermal-Hydraulic Design of High-Power-Density Annular Fuel in PWRs THERMAL-HYDRAULIC DESIGN OF HIGH-POWER-DENSITY ANNULAR FUEL IN PWRs MANAGEMENT’, 5450(August).

Flownex SE (2022) ‘Flownex Library Manual’, (March).

Gabr, F. A. *et al.* (2003) ‘Pressure and Composition of Gas Mixtures in Fuel Rods for Pressurised Water Reactors by an Ultrasonic Sensor’, *International Conference on WWER Fuel performance, Modelling and Experimental Support*, pp. 278–284. Available at: https://inis.iaea.org/search/search.aspx?orig_q=RN:36040522.

Hejzlar, P. and Kazimi, M. S. (2007) ‘Annular fuel for high-power-density pressurized water reactors: Motivation and overview’, *Nuclear Technology*, 160(1), pp. 2–15. doi: 10.13182/NT160-2-15.

Hejzlar, P. and Kazimi, M. S. (2008) *Final Technical Report for the MIT Annular Fuel Research Project - Page 14 of 19 - UNT Digital Library*. Available at: https://digital.library.unt.edu/ark:/67531/metadc898863/m1/14/ (Accessed: 29 October 2020).

Horelik *et al.* (2018) ‘Benchmark for Evaluation And Validation of Reactor Simulations, RELEASE rev. 2.0.2’, pp. 1–177.

IAEA (2014) *Accident Tolerant Fuel Concepts for Light Water Reactors | IAEA*. Available at: https://www.iaea.org/publications/10972/accident-tolerant-fuel-concepts-for-light-water-reactors (Accessed: 6 April 2022).

IAEA (2015) *THE FUKUSHIMA DAIICHI ACCIDENT REPORT BY THE DIRECTOR GENERAL*.

IEA (2021) *Net Zero by 2050 – Analysis - IEA*, *International Energy Agency*. Available at: https://www.iea.org/reports/net-zero-by-2050 (Accessed: 21 June 2021).

IRP (2019) ‘Integrated Resource Plan (IRP2019)’, *Integrated Resource Plan*.

Jiang, W. *et al.* (2021) ‘TRISO particle fuel performance and failure analysis with BISON’, *Journal of Nuclear Materials*, 548, p. 152795. doi: 10.1016/j.jnucmat.2021.152795.

Kaltiaisenaho, T. (2020) ‘Photon transport physics in Serpent 2 Monte Carlo code ☆’, *Computer Physics Communications*, 252, p. 107143. doi: 10.1016/j.cpc.2020.107143.

Kavazauri, R. *et al.* (2016) ‘Thermal properties of nonstoichiometry uranium dioxide’, *IOP Conference Series: Materials Science and Engineering*, 130(1). doi: 10.1088/1757-899X/130/1/012025.

Kazimi, M. S. and Hejzlar, P. (2006) ‘High Performance Fuel Design for next generation PWR’s’.

Kianpour, R. *et al.* (2020) ‘Optimal design of a VVER-1000 nuclear reactor core with dual cooled annular fuel based on the reactivity temperature coefficients using Thermal hydraulic and neutronic analysis by implementing the genetic algorithms’. doi: 10.1016/j.anucene.2020.107682.

Koo, Y. H. *et al.* (2014) ‘Kaeri’s development of LWR accident-tolerant fuel’, *Nuclear Technology*, 186(2), pp. 295–304. doi: 10.13182/NT13-89.

Lamarsh and Baratta (2001) *Introcution to Nuclear Engineering*, *Prentice hall*.

Leppänen, J. (2010) ‘20th AER Symposium on VVER Reactor Physics and Reactor Safety’, (September), pp. 1–13. Available at: http://ttuki.vtt.fi/serpent.

Leppänen, J. *et al.* (2014) ‘Annals of Nuclear Energy The Serpent Monte Carlo code : Status , development and applications in 2013’, 2007. doi: 10.1016/j.anucene.2014.08.024.

Li, B.-S. (2013) ‘Pellet cladding mechanical interactions of ceramic claddings fuels under light water reactor conditions’, (January 2013), p. 116. doi: 10.13140/2.1.2970.3204.

Liu, S. and Cai, J. (2013) ‘Convergence analysis of neutronic/thermohydraulic coupling behavior of SCWR’, *Nuclear Engineering and Design*, 265, pp. 53–62. doi: 10.1016/j.nucengdes.2013.06.017.

Lodi, F. *et al.* (2016) ‘ANTEO+: A subchannel code for thermal-hydraulic analysis of liquid metal cooled systems’, *Nuclear Engineering and Design*, 301, pp. 128–152. doi: 10.1016/j.nucengdes.2016.03.001.

Mozafari, M. A. and Faghihi, F. (2013) ‘Annals of Nuclear Energy Design of annular fuels for a typical VVER-1000 core : Neutronic investigation , pitch optimization and MDNBR calculation q’, *ANNULS OF NUCLEAR ENERGY*, 60, pp. 226–234. doi: 10.1016/j.anucene.2013.04.035.

Mulasi, C. (2022) *Criticality study of a spent fuel pool using SCALE 6.2.3 and MCNP6.2*. Available at: https://repository.nwu.ac.za/bitstream/handle/10394/40143/Mulasi, C.pdf?sequence=1.

NEA (2022) *Reference Values for Nuclear Criticality Safety*. Available at: https://www.oecd-nea.org/science/wpncs/Publications/ref-val-criticality-safety/ (Accessed: 21 August 2022).

Nuclear power (2021) *Accident Tolerant Fuel | Types & Advantages | nuclear-power.net*. Available at: https://www.nuclear-power.net/nuclear-power-plant/nuclear-fuel/accident-tolerant-fuel-atf/ (Accessed: 7 June 2021).

Nuclear power (2022a) *Fuel Burnup | Definition, Calculation & Units | nuclear-power.com*. Available at: https://www.nuclear-power.com/nuclear-power/reactor-physics/reactor-operation/fuel-burnup/ (Accessed: 30 May 2022).

Nuclear power (2022b) *Reactivity | Definition & Calculation | nuclear-power.com*. Available at: https://www.nuclear-power.com/nuclear-power/reactor-physics/nuclear-fission-chain-reaction/reactivity/ (Accessed: 21 November 2022).

Nuclear power (2022c) *Self-shielding - Energy and Spatial | nuclear-power.com*. Available at: https://www.nuclear-power.com/nuclear-power/reactor-physics/nuclear-engineering-fundamentals/neutron-nuclear-reactions/self-shielding/ (Accessed: 18 November 2022).

Nuclear power (2022d) *Temperature Profile - Nuclear Fuel*. Available at: https://www.nuclear-power.com/nuclear-engineering/heat-transfer/heat-generation/temperature-profile-nuclear-fuel/ (Accessed: 9 May 2022).

Nuclear power (2022e) *Thermal Conductivity of Uranium Dioxide*. Available at: https://www.nuclear-power.com/nuclear-engineering/heat-transfer/thermal-conduction/thermal-conductivity/thermal-conductivity-of-uranium-dioxide/ (Accessed: 7 May 2022).

Nuclear power (2022f) *Zirconium - Melting Point - Boiling Point | nuclear-power.com*. Available at: https://www.nuclear-power.com/zirconium-melting-point-boiling-point/ (Accessed: 17 October 2022).

Nuclear power (2022g) *Zirconium Alloy – Zircaloy – 4*. Available at: https://www.nuclear-power.com/nuclear-engineering/metals-what-are-metals/alloys-composition-properties-of-metal-alloys/zirconium-alloys/zirconium-alloy-zircaloy-4/ (Accessed: 25 February 2023).

Nuclear Power South Africa (2021) *Nuclear Power in South Africa | South African Nuclear Energy - World Nuclear Association*. Available at: https://world-nuclear.org/information-library/country-profiles/countries-o-s/south-africa.aspx (Accessed: 2 June 2021).

Otto et al. (2014) 'Preliminary assessment of accident-tolerant fuels on LWR performance during normal operation and under DB and BDB accident conditions', *Journal of Nuclear Materials*, 448(1–3), pp. 520–533. doi: 10.1016/j.jnucmat.2013.09.052.

Pane, D. N. *et al.* (2018) 'MODELING APPROACH FOR ANNULAR-FUEL ELEMENTS USING THE ASSERT-PV SUBCHANNEL CODE', *Journal of Chemical Information and Modeling*, 53(9), pp. 1689–1699.

Popov *et al.* (2000) 'Thermophysical Properties of MOX and UO2 Fuels Including the Effects of Irradiation', 0.

Van Ravenswaay, J. P. *et al.* (2006) 'Verification and validation of the HTGR systems CFD code Flownex', *Nuclear Engineering and Design*, 236(5–6), pp. 491–501. doi: 10.1016/j.nucengdes.2005.11.025.

Rebak, R. B. (2020) 'Silicon carbide and ceramics metal composite', in *Accident Tolerant Materials for Light Water Reactor Fuels*. Elsevier, pp. 143–156. doi: 10.1016/b978-0-12-817503-3.00006-7.

Safavi, A. *et al.* (2020) 'Application of a new neutronics / thermal-hydraulics coupled code for steady state analysis of light water reactors', *Nuclear Engineering and Technology*, 52(8), pp. 1603–1610. doi: 10.1016/j.net.2020.01.024.

Sargent, R. G. (2013) 'Verification and validation of simulation models', *Journal of Simulation*, 7(1), pp. 12–24. doi: 10.1057/jos.2012.20.

Silva, R. H. M. *et al.* (2017) 'NEUTRONIC EVALUATION OF ANNULAR FUEL RODS TO ASSEMBLIES 13X13 , 14X14 AND 15X15 .'

Singh, G. *et al.* (2018) 'Parametric Evaluation of SiC/SiC Composite Cladding with UO2 Fuel for LWR Applications: Fuel Rod Interactions and Impact of Nonuniform Power Profile in Fuel Rod', *Journal of Nuclear Materials*, 499, pp. 155–167. doi: 10.1016/j.jnucmat.2017.10.059.

Slabber, J. (2014) ‘Is silicon carbide a solution to safer light-water reactor fuel?’, *Innovate*, pp. 48–51. Available at: https://www.up.ac.za/media/shared/404/ZP_Files/Innovate 09/Articles/is-silicon-carbide-a-solution-to-safer-light-water-reactor-fuel_slabber.zp40149.pdf.

Stacey, W. M. (2007) *Nuclear Reactor Physics: Second Edition*, *Nuclear Reactor Physics: Second Edition*. doi: 10.1002/9783527611041.

Statistics South Africa (2021) *Statistics South Africa/ Energy*, *Statistics South Africa*. Available at: http://www.statssa.gov.za/?cat=38 (Accessed: 8 March 2021).

Terrani, K. A. *et al.* (2015) ‘Hydrothermal corrosion of SiC in LWR coolant environments in the absence of irradiation *’, *Journal of Nuclear Materials*, 465, pp. 488–498. doi: 10.1016/j.jnucmat.2015.06.019.

Terrani, K. A. (2018) ‘Accident tolerant fuel cladding development: Promise, status, and challenges’, *Journal of Nuclear Materials*. Elsevier B.V., pp. 13–30. doi: 10.1016/j.jnucmat.2017.12.043.

du Toit, M. H. (2017) ‘Analysis of specific design aspects of a thorium-uranium fuelled European Pressurised Reactor’, pp. 1–130. doi: 10.13140/RG.2.2.10600.62722.

VEPCO (2016) *‘North Anna Power Station Updated Final Safety Analysis Report Chapter4’.* Virginia Electric and Power Company Richmon, Virginia 2361: United States Nuclear Regulatory Commision.

Wang, L. *et al.* (2017) ‘Development of SNTA code system for SCWR core steady-state analysis’, *Journal of Nuclear Engineering and Radiation Science*, 3(2). doi: 10.1115/1.4035334.

Weaver, K. D. and Herring, J. S. (2002) ‘THE EFFECT OF THE HYDROGEN TO HEAVY METAL RATIO (H/HM) ON REACTIVITY AND DISCHARGE ISOTOPICS OF HOMOGENEOUS THORIA-URANIA FUEL’, in *10TH International Conference on Nuclear Engineering*. Idaho, pp. 251–257. doi: 10.1115/ICONE10-22070.

Yapici, H. (2002) ‘Temperature distribution in nuclear fuel rod and variation of the neutronic performance parameters in (D–T) driven hybrid reactor system’, *Fuel and Energy Abstracts*, 43(4), p. 258. doi: 10.1016/s0140-6701(02)86269-5.

Yarmohammadi, M. *et al.* (2017) ‘Effect of central hole on fuel temperature distribution’, *Nuclear Engineering and Technology*, 49(8), pp. 1629–1635. doi: 10.1016/j.net.2017.07.022.

Ye, L. *et al.* (2020) ‘Thermal hydraulic and neutronics coupling analysis for plate type fuel in nuclear reactor core’, *Science and Technology of Nuclear Installations*, 2020. doi: 10.1155/2020/2562747.

Young, G. A. *et al.* (2012) *Welds for Nuclear Systems*, *Comprehensive Nuclear Materials*. Elsevier Inc. doi: 10.1016/B978-0-08-056033-5.00089-6.

Yueh, K. and Terrani, K. A. (2014) ‘Silicon carbide composite for light water reactor fuel assembly applications’, *Journal of Nuclear Materials*, 448(1–3), pp. 380–388. doi: 10.1016/j.jnucmat.2013.12.004.

# APPENDICES

## 7.1 Appendix A: Material properties

Material number densities for all the materials are calculated using Equation **3-3**. The three models use different fuel $UO_2$ enrichment and cladding.

**Table 7-1: Solid reference pin fuel enrichment**

| 3.10% fuel enrichment | | | | | | |
|---|---|---|---|---|---|---|
| **Serpent mat** | **Isotope** | **Mass (M)** | **Abundance** | **Atom density** | **atom/b-cm** | **Atom fraction** |
| 8016 | O16 | 15.99 | 9.98E-01 | 2.32E+24 | 4.64E+00 | 6.65E-01 |
| 8017 | O17 | 16.99 | 3.80E-04 | 8.82E+20 | 1.76E-03 | 2.53E-04 |
| 8018 | O18 | 17.99 | 2.00E-03 | 4.64E+21 | 9.29E-03 | 1.33E-03 |
| 92234 | U234 | 234.04 | 3.23E-04 | 5.76E+20 | 5.76E-04 | 8.26E-05 |
| 92235 | U235 | 235.04 | 4.04E-02 | 7.20E+22 | 7.20E-02 | 1.03E-02 |
| 92238 | U238 | 238.05 | 9.60E-01 | 2.25E+24 | 2.25E+00 | 3.22E-01 |

**Table 7-2: Water annulus fuel enrichment**

| 3.40% fuel enrichment | | | | | | |
|---|---|---|---|---|---|---|
| **Serpent mat** | **Isotope** | **Mass (M)** | **Abundance** | **Atom density** | **atom/b-cm** | **Atom fraction** |
| 8016 | O16 | 15.99 | 9.98E-01 | 2.29E+24 | 4.58E+00 | 6.65E-01 |
| 8017 | O17 | 16.99 | 3.80E-04 | 8.73E+20 | 1.75E-03 | 2.53E-04 |
| 8018 | O18 | 17.99 | 2.00E-03 | 4.60E+21 | 9.19E-03 | 1.33E-03 |
| 92234 | U234 | 234.04 | 3.23E-04 | 6.26E+20 | 6.26E-04 | 9.09E-05 |
| 92235 | U235 | 235.04 | 4.04E-02 | 7.83E+22 | 7.83E-02 | 1.14E-02 |
| 92238 | U238 | 238.05 | 9.60E-01 | 2.22E+24 | 2.22E+00 | 3.22E-01 |

**Table 7-3: Helium annulus fuel enrichment**

| 4.04% fuel enrichment | | | | | | |
|---|---|---|---|---|---|---|
| **Serpent mat** | **Isotope** | **Mass (M)** | **Abundance** | **Atom density** | **atom/b-cm** | **Atom fraction** |
| 8016 | O16 | 15.99 | 9.98E-01 | 2.29E+24 | 4.58E+00 | 6.65E-01 |
| 8017 | O17 | 16.99 | 3.80E-04 | 8.73E+20 | 1.75E-03 | 2.53E-04 |
| 8018 | O18 | 17.99 | 2.00E-03 | 4.60E+21 | 9.19E-03 | 1.33E-03 |
| 92234 | U234 | 234.04 | 2.98E-04 | 7.43E+20 | 7.43E-04 | 1.08E-04 |
| 92235 | U235 | 235.04 | 3.73E-02 | 9.29+22 | 9.29E-02 | 1.35E-02 |
| 92238 | U238 | 238.05 | 9.66E-01 | 2.20E+24 | 2.20E+00 | 3.20E-01 |

**Table 7-4: Helium annulus fuel enrichment**

| 3.10% fuel enrichment | | | | | | |
|---|---|---|---|---|---|---|
| **Serpent mat** | **Isotope** | **Mass (M)** | **Abundance** | **Atom density** | **atom/b-cm** | **Atom fraction** |
| 8016 | O16 | 15.99 | 9.98E-01 | 2.30E+20 | 4.59E-04 | 6.65E-01 |
| 8017 | O17 | 16.99 | 3.80E-04 | 8.73E+16 | 1.75E-07 | 2.53E-04 |
| 8018 | O18 | 17.99 | 2.00E-03 | 4.60E+17 | 9.19E-07 | 1.33E-03 |
| 92234 | U234 | 234.04 | 2.98E-04 | 5.70E+16 | 5.70E-08 | 8.26E-05 |
| 92235 | U235 | 235.04 | 3.73E-02 | 7.13+18 | 7.13E-06 | 1.03E-02 |
| 92238 | U238 | 238.05 | 9.66E-01 | 2.23E+20 | 2.23E-04 | 3.23E-01 |

**Table 7-5: SiC material composition**

| **Serpent mat** | **Isotope** | **Mass (M)** | **Abundance** | **Atom density** | **atom/b-cm** | **Atom fraction** |
|---|---|---|---|---|---|---|
| **14028** | Si-28 | 27.98 | 9.22E-01 | 4.43E+22 | 4.43E-02 | 4.61E-01 |
| **14029** | Si-29 | 28.98 | 4.68E-02 | 2.25E+21 | 2.25E-03 | 2.34E-02 |
| **14030** | Si-30 | 29.97 | 3.09E-02 | 1.48E+21 | 1.48E-03 | 1.54E-02 |
| **6012** | C-12 | 12.00 | 9.89E-01 | 4.75E+22 | 4.75E-02 | 4.94E-01 |
| **6013** | C-13 | 13.00 | 1.11E-02 | 5.32E+20 | 5.32E-04 | 5.53E-03 |

## 7.2 Appendix B: Helium annulus 3.1 wt % enrichment results

Section 5.1.1 results are presented in this appendix. The fuel pin and assembly results are listed in Table 7-6 and the Figure 7-1 and Figure 7-2 show the variation of burnup with $k_{eff}$.

**Table 7-6: Burnup results**

| | BOL ($k_{eff}$) | EOL ($k_{eff}$)) | Burnup (MWd/kgU) | Cycle length (EFPD) |
|---|---|---|---|---|
| **Fuel pin** | | | | |
| **Helium annulus** | 1.2721 | 0.8137 | 75.0 | 1445.6 |
| **Reference** | 1.3071 | 0.8140 | 66.3 | 1676.9 |
| **Difference** | -0.0349 | -0.0003 | 8.8 | -231.3 |
| **Fuel assembly** | | | | |
| **Helium annulus** | 1.2934 | 0.7974 | 76.3 | 1461.7 |
| **Reference** | 1.3317 | 0.7978 | 66.3 | 1675.6 |
| **Difference** | -0.0383 | -0.0004 | 10.0 | -213.9 |

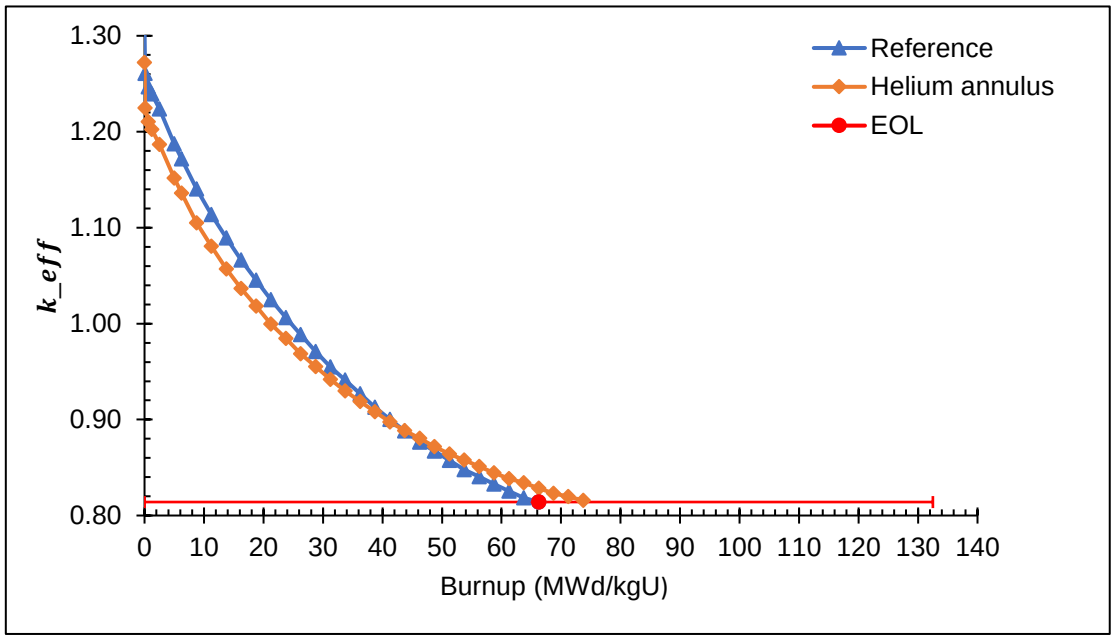


**Figure 7-1: Variation of $k_{eff}$ with burnup for fuel pins**

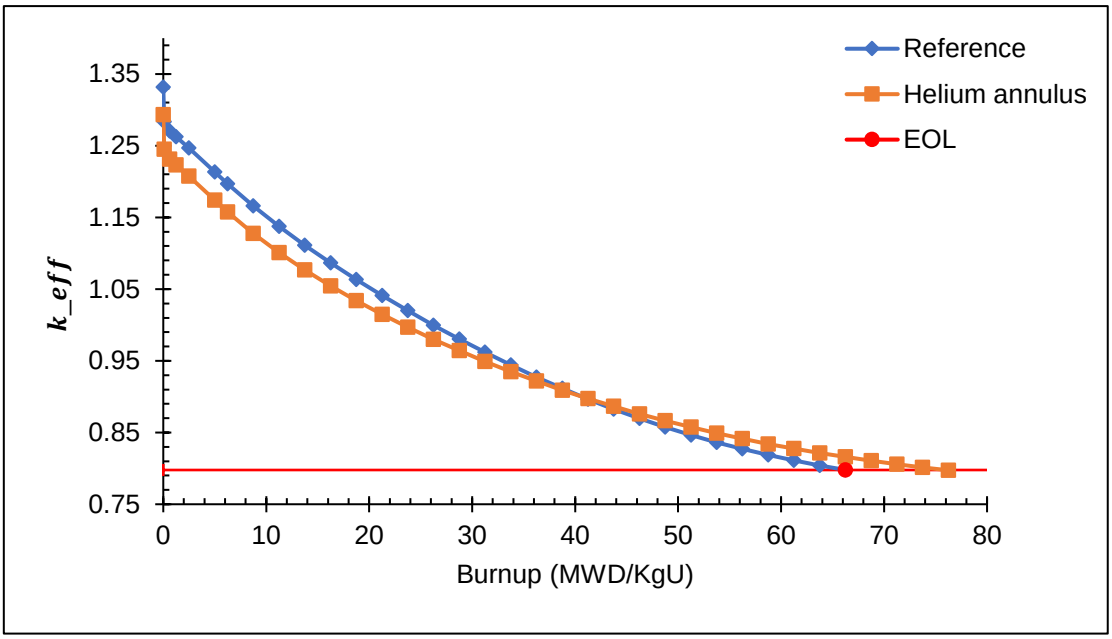


**Figure 7-2: Variation of $k_{eff}$ with burnup for the fuel assemblies**

## 7.3 Appendix C: Shannon entropy

Shannon entropy plots for the fuel pins and assemblies for the three models are provided as validation for convergence for Section 4.6.3.

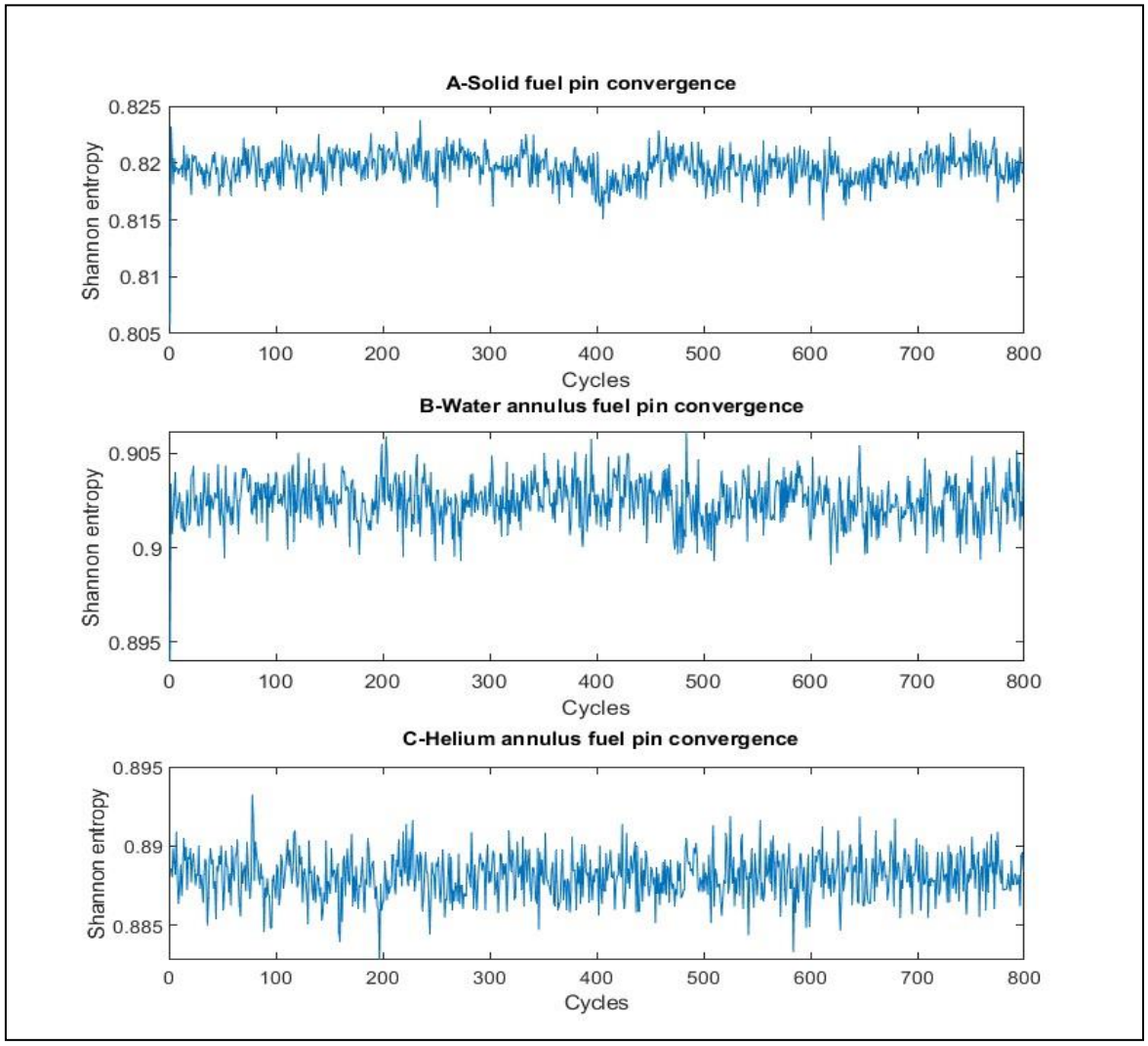


**Figure 7-3: Fuel pin Shannon entropy**

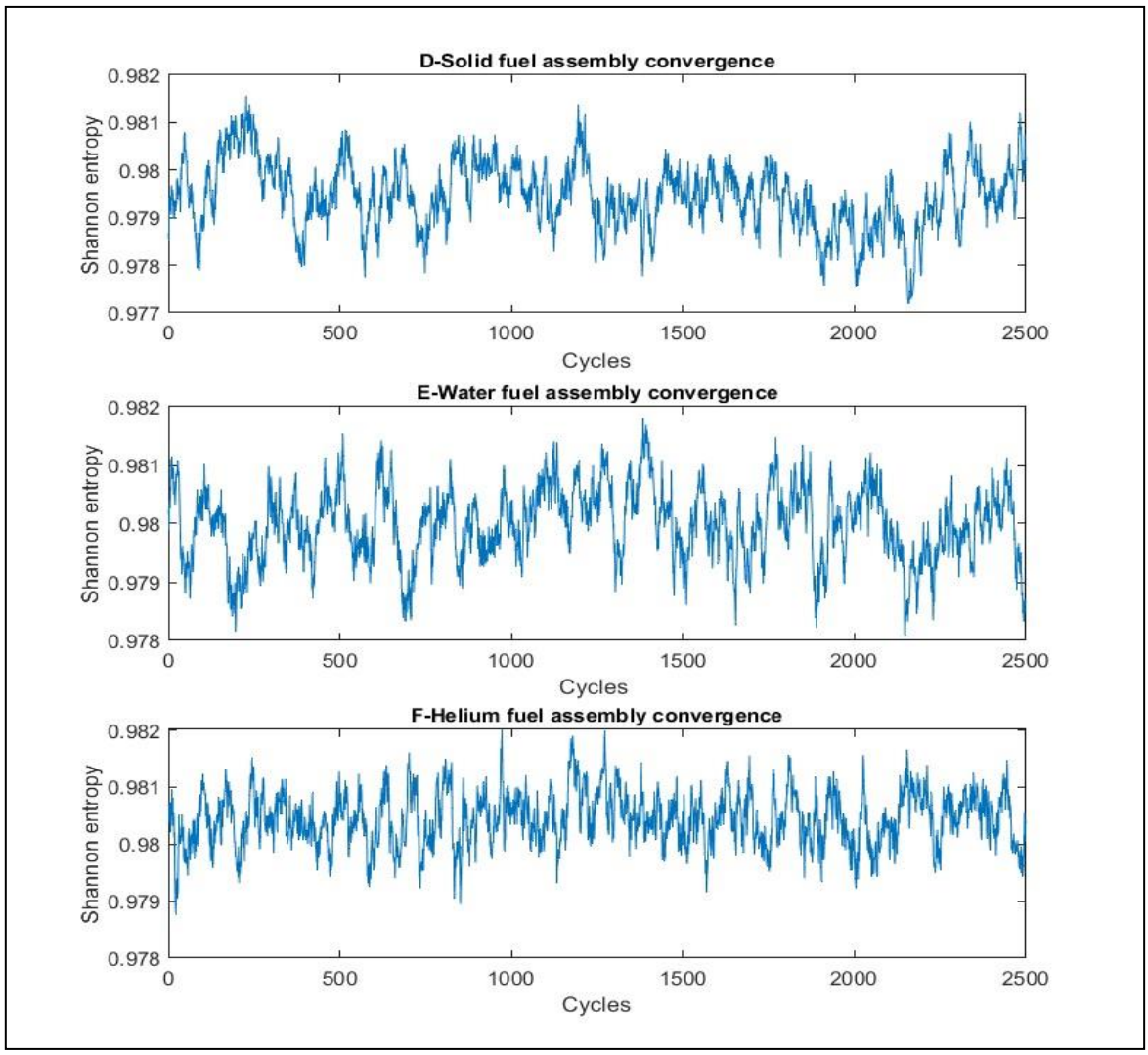


**Figure 7-4: Fuel assembly Shannon entropy**

## 7.4 Appendix D: Serpent coupling input files

Table 7-7 to Table 7-9 show the 3D, cool.ifc and fuel.ifc input files for Serpent as discussed in the coupling methodology Section 4.5.

**Table 7-7: Serpent 3D input**

```
set title "Ref-pin"



set acelib "/share/apps/Serpent2020/xsdata/endfb7/sss_endfb7u.xsdata"

set declib "/share/apps/Serpent2020/xsdata/endfb7/sss_endfb7.dec"

set nfylib "/share/apps/Serpent2020/xsdata/endfb7/sss_endfb7.nfy"



% --- Material definitions

% --- 3.10221 wt-% enriched uranium dioxide fuel

%     Density of the fuel 10.41200 g/cm3

mat fuel   -10.41200 tft 500 2000 rgb 255 250 100

92234.03c    8.26086E-05

92235.03c    1.03261E-02

92238.03c    3.22536E-01

 8016.03c    6.67055E-01



% --- Clad material Zircaloy4

%     Density 6.55000 g/cm3

mat Zircaloy4 -6.55000 rgb 100 100 100

24000.03c  -9.97000E-04

26000.03c  -1.99400E-03

40000.03c  -9.81858E-01

50000.03c  -1.39550E-02

 8016.03c  -2.38876E-03

 8017.03c  -3.24113E-06

24050.03c  -4.16117E-05

24052.03c  -8.34483E-04

24053.03c  -9.64457E-05
```

```
24054.03c  -2.44600E-05

26054.03c  -1.12572E-04

26056.03c  -1.83252E-03

26057.03c  -4.30778E-05

26058.03c  -5.83334E-06

40090.03c  -4.97862E-01

40091.03c  -1.09780E-01

40092.03c  -1.69646E-01

40094.03c  -1.75665E-01

40096.03c  -2.89038E-02

50112.03c  -1.27604E-04

50114.03c  -8.83732E-05

50115.03c  -4.59255E-05

50116.03c  -1.98105E-03

50117.03c  -1.05543E-03

50118.03c  -3.35688E-03

50119.03c  -1.20069E-03

50120.03c  -4.59220E-03

50122.03c  -6.63497E-04

50124.03c  -8.43355E-04


% --- Void material Helium

mat helium  -0.000166 tmp 700.023194 rgb 255 255 255

 2003.03c    2.00004E-06

 2004.03c    9.99998E-01


mat cool -0.70410 tft 500 900 moder lwtr 1001 rgb 200 200 250

 8016.03c   1.0

 1001.03c   2.0

% --- Thermal scattering data for light water:

%     On-the-fly treatment for SAB-data between 474 K -- 1000 K

therm lwtr 0 lwj3.00t lwj3.01t lwj3.03t lwj3.05t lwj3.07t lwj3.09t lwj3.11t lwj3.13t lwj3.14t lwj3.18t
lwj3.20t
```

```
% -- Geometry definitions

% --- Fuel pin

pin 1

fuel          0.40958

void          0.41783

Zircaloy4  0.47498

cool

set ufs 3 1 5 -0.40958 +0.40958 5 -0.40958 +0.40958 10 -182.499 182.499

% --- Lattice (type = 1, pin pitch = 1.25984):

lat 10  1  0.0 0.0 1 1 1.25984

1

% -- Run parameters

set pop 25000 800 450

set bc 2 2 1

set fsp 1 20

set gcu -1

set power 69798.301486

set relfactor 0.3

set entr 5 5 5 -0.62992  0.62992 -0.62992  0.62992 -182.499 182.499

set his 1

set mcvol 1000000


surf 1 cylz 0.0 0.0 0.40958 -182.499 182.499

surf 2 cylz 0.0 0.0 0.41783 -182.499 182.499

surf 3 cylz 0.0 0.0 0.47498 -182.499 182.499

surf 4 pz -182.499

surf 5 pz 182.499

surf 6 cuboid -0.62992 0.62992 -0.62992 0.62992 -182.499 182.499


%cell 2 1 fuel -1

%cell 3 1 helium -2 1

%cell 4 1 Zircaloy4 -3 2
```

```
%cell 5 1 cool 3

cell 6 0 fill 1 -6  4 -5

cell 7 0 outside 6

% --- Geometry plots

% --- XY-plot

plot 3 2000 2000 %0 -1 1 -1 1

plot 2 2000 5000

% --- XY-meshplot

mesh 3  2000  2000

mesh 2  2000  5000

% --- Temp meshplot

mesh 10 3 2000 2000

mesh 10 2 2000 5000


ifc fuel.ifc setmat 1 fuel

ifc Cool.ifc setmat 1 cool
```

**Table 7-8: Serpent cool.ifc input**

```
2 cool 1

coolifc.out 10 -182.499 182.499 1

1

1 -0.62992 0.62992 1 -0.62992 0.62992 10 -182.499 182.499

-0.75085  560.55325

-0.74237  564.99111

-0.72917  571.59776

-0.71416  578.60264

-0.69943  585.04974

-0.68603  590.54560

-0.67446  595.01167

-0.66504  598.45470

-0.65813  600.86157

-0.65427  602.16101
```

**Table 7-9: Serpent fuel.ifc input**

```
6 fuel.ifcout 1

1

10 -182.499 182.499 1 0 360 5 0 0.40958

10 -182.499 182.499 1 0 360 5 0 0.40958 1.00E-11 20.0

10

-182.499 -145.99920 1

0 360 7

0.00000   0.00000 920.2150927

0.07447   0.07447 843.0339926

0.14894   0.14894 825.375822

0.22341   0.22341 797.444412

0.29788   0.29788 760.0341994

0.37235   0.37235 714.251897

0.40958   0.40958 687.3542947

-145.99920 -109.49940  1

0 360 7

0.00000   0.00000 1580.143934

0.07447   0.07447 1306.006518

0.14894   0.14894 1247.891796

0.22341   0.22341 1159.506106

0.29788   0.29788 1047.176025

0.37235   0.37235 918.2270736

0.40958   0.40958 851.8610039

-109.49940 -72.99960 1

0 360 7

0.00000   0.00000 2123.196541

0.07447   0.07447 1691.213328

0.14894   0.14894 1596.856194

0.22341   0.22341 1454.793638

0.29788   0.29788 1278.491288

0.37235   0.37235 1082.608452
```

0.40958 0.40958 991.9323825

-72.99960 -36.49980 1

0 360 7

0.00000 0.00000 2313.487461

0.07447 0.07447 1839.930794

0.14894 0.14894 1731.547474

0.22341 0.22341 1567.406008

0.29788 0.29788 1364.197448

0.37235 0.37235 1140.826996

0.40958 0.40958 1040.31175

-36.49980 0 1

0 360 7

0.00000 0.00000 2311.105609

0.07447 0.07447 1842.909824

0.14894 0.14894 1735.594743

0.22341 0.22341 1572.864943

0.29788 0.29788 1371.056339

0.37235 0.37235 1148.839011

0.40958 0.40958 1048.99714

0 36.49980 1

0 360 7

0.00000 0.00000 2159.363387

0.07447 0.07447 1730.686841

0.14894 0.14894 1635.713232

0.22341 0.22341 1492.18626

0.29788 0.29788 1313.508442

0.37235 0.37235 1114.749656

0.40958 0.40958 1024.14357

36.49980 72.99960 1

0 360 7

0.00000 0.00000 1843.841823

0.07447 0.07447 1509.121218

0.14894 0.14894 1437.594905

0.22341 0.22341 1329.240484

0.29788 0.29788 1192.60036

0.37235 0.37235 1037.153171

0.40958 0.40958 963.4736142

72.99960 109.49940 1

0 360 7

0.00000 0.00000 1453.0053

0.07447 0.07447 1243.910561

0.14894 0.14894 1198.549488

0.22341 0.22341 1128.727836

0.29788 0.29788 1038.461261

0.37235 0.37235 932.6163539

0.40958 0.40958 879.1143549

109.49940 145.99920 1

0 360 7

0.00000 0.00000 1044.861163

0.07447 0.07447 943.8753167

0.14894 0.14894 921.0464033

0.22341 0.22341 885.1496694

0.29788 0.29788 837.4239215

0.37235 0.37235 779.5555477

0.40958 0.40958 746.7954807

145.99920 182.499 1

0 360 7

0.00000 0.00000 752.4700008

0.07447 0.07447 722.5270755

0.14894 0.14894 715.4592762

0.22341 0.22341 704.1035718

0.29788 0.29788 688.5715039

0.37235 0.37235 669.0892111

0.40958 0.40958 657.2891791

## 7.5 Appendix E: Flownex output files

Table 7-10 shows coolant temperature and density, and Figure 7-5 depicts the fuel and cladding temperature.

**Table 7-10: Flownex coolant output**

| 1st iteration | | | |
|---|---|---|---|
| **increment** | **den (g/cm3)** | **SER density** | **T (K)** |
| 1 | 753.53312 | -0.75353 | 559.80513 |
| 2 | 749.23243 | -0.74923 | 562.07309 |
| 3 | 741.63550 | -0.74164 | 566.06412 |
| 4 | 731.07923 | -0.73108 | 571.34505 |
| 5 | 718.18065 | -0.71818 | 577.47632 |
| 6 | 703.60038 | -0.70360 | 583.95133 |
| 7 | 688.35046 | -0.68835 | 590.21192 |
| 8 | 673.92014 | -0.67392 | 595.64199 |
| 9 | 662.23006 | -0.66223 | 599.67132 |
| 10 | 655.25324 | -0.65525 | 601.88816 |

| | | 1st iteration | | | | | | | | | | |
|---|---|---|---|---|---|---|---|---|---|---|---|---|
| | z increme | 1 | 2 | 3 | 4 | 5 | 6 | 7 | 8 | 9 | 10 | |
| | r nodes | | | | | | | | | | | |
| 0.00000 | 1 | 920.2151 | 1580.144 | 2123.197 | 2313.487 | 2311.106 | 2159.363 | 1843.842 | 1453.005 | 1044.861 | 752.47 | |
| 0.07447 | 2 | 843.034 | 1306.007 | 1691.213 | 1839.931 | 1842.91 | 1730.687 | 1509.121 | 1243.911 | 943.8753 | 722.5271 | |
| 0.14894 | 3 | 825.3758 | 1247.892 | 1596.856 | 1731.547 | 1735.595 | 1635.713 | 1437.595 | 1198.549 | 921.0464 | 715.4593 | |
| 0.22341 | 4 | 797.4444 | 1159.506 | 1454.794 | 1567.406 | 1572.865 | 1492.186 | 1329.24 | 1128.728 | 885.1497 | 704.1036 | |
| 0.29788 | 5 | 760.0342 | 1047.176 | 1278.491 | 1364.197 | 1371.056 | 1313.508 | 1192.6 | 1038.461 | 837.4239 | 688.5715 | |
| 0.37235 | 6 | 714.2519 | 918.2271 | 1082.608 | 1140.827 | 1148.839 | 1114.75 | 1037.153 | 932.6164 | 779.5555 | 669.0892 | |
| 0.40958 | 7 | 687.3543 | 851.861 | 991.9324 | 1040.312 | 1048.997 | 1024.144 | 963.4736 | 879.1144 | 746.7955 | 657.2892 | |
| | | | | | | | | | | | | |
| | | **Gap temp K** | | | | | | | | | | |
| | 8 | 634.0502 | 727.5947 | 831.8987 | 866.0156 | 876.6584 | 866.8452 | 833.1178 | 781.6394 | 683.685 | 633.8596 | 773.5365 |
| | | **Clad temp K** | | | | | | | | | | |
| | 9 | 571.5401 | 589.6403 | 664.3733 | 687.6261 | 701.7198 | 705.9239 | 696.6643 | 676.6129 | 612.2446 | 606.4439 | 651.2789 |
| | | | | | | | | | | | | |
| | | Maximum fuel cetreli | 2313.487 | | | | | | | | | |
| | | Maximum cladding su | 705.9239 | | | | | | | | | |

**Figure 7-5: Flownex output file**

## 7.6 Appendix F: Fuel temperature profiles

Figure 7-6 shows temperature profiles of the solid reference pin, and Figure 7-7 shows that of the helium annulus pin.

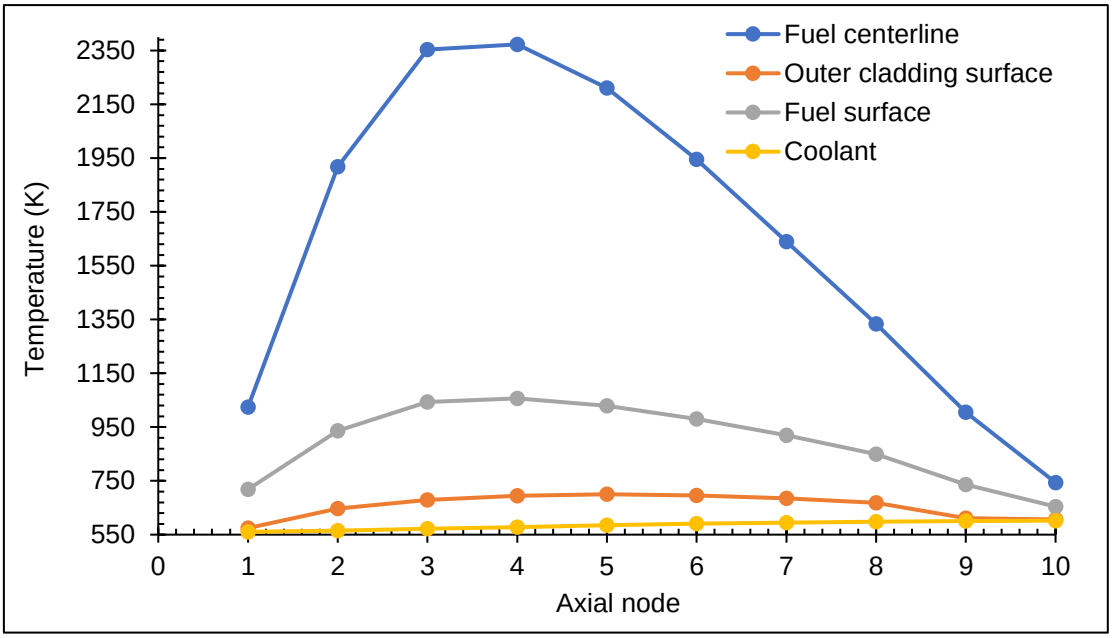


**Figure 7-6: Temperature profiles of the solid reference pin**

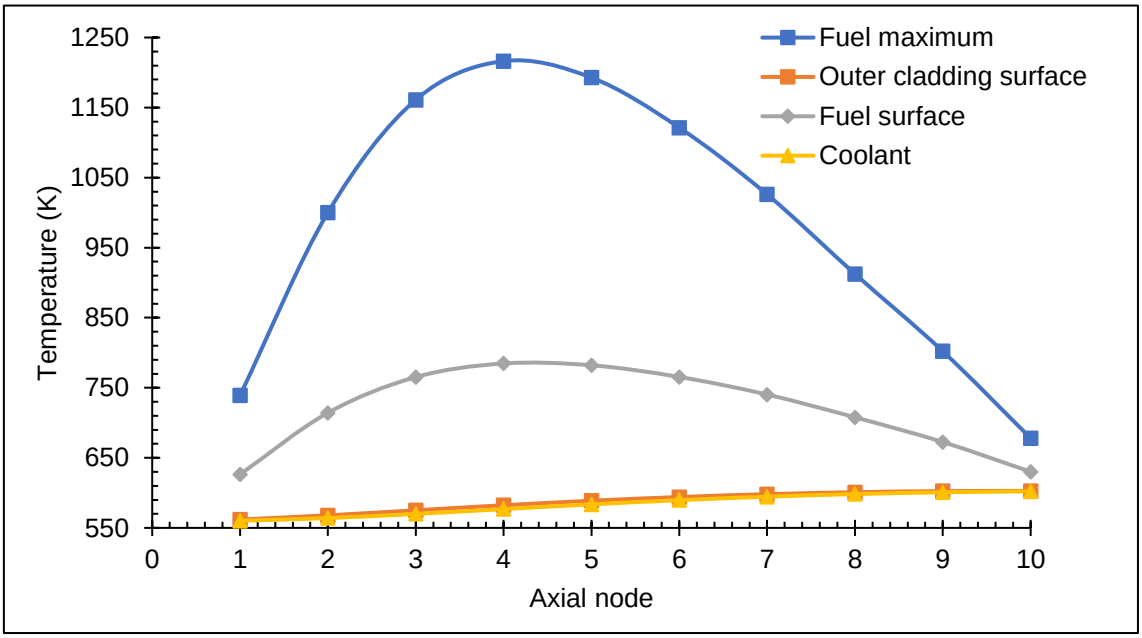


**Figure 7-7: Temperature profiles of the helium annuls pin**